Lawrence Berkeley National Laboratory

Title
Using onset times from frequent geophysical surveys to understand reservoir fluid flow and to estimate flow properties

Permalink
https://escholarship.org/uc/item/9zk0n0h3

Journal
First Break, 39(2)

ISSN
0263-5046

Authors
Vasco, Donald W
Hetz, Gil
Datta-Gupta, Akhil

Publication Date
2021-02-01

DOI
10.3997/1365-2397.fb2021011

Peer reviewed

USING ONSET TIMES FROM FREQUENT SEISMIC SURVEYS TO UNDERSTAND

FLUID FLOW AT THE PEACE RIVER FIELD, CANADA

Gil Hetz, Akhil Datta-Gupta, Texas A&M University

Justyna K. Przybysz-Jarnut, Jorge L. Lopez, Shell International

and D. W. Vasco, Lawrence Berkeley National Laboratory

ABSTRACT

Our limited knowledge of the relationship between changes in the state of an aquifer or reservoir and the corresponding changes in the elastic moduli, that is the rock physics model, hampers the effective use of time-lapse seismic observations for estimating flow properties within the Earth. A central problem is the complicated dependence of the magnitude of time-lapse changes on the saturation, pressure, and temperature changes within an aquifer or reservoir. We describe an inversion methodology for reservoir characterization that uses onset times, the calendar time of the change in seismic attributes, rather than the magnitude of the changes. We find that onset times are much less sensitive than magnitudes to the rock physics model used to relate time-lapse observations to changes in saturation, temperature and fluid pressure. We apply the inversion scheme to observations from daily monitoring of enhanced oil recovery at the Peace River field in Canada. An array of 1492 buried hydrophones record seismic signals from 49 buried sources. Time shifts for elastic waves traversing the reservoir are extracted from the daily time-lapse cubes. In our analysis 175 images of time shifts are transformed into a single map of onset times, leading to a substantial reduction in the volume of data. These observations are used in conjunction with bottom hole pressure data to infer the initial conditions prior to the injection, and to update the reservoir permeability model. The combination of a global and local inversion scheme produces a collection of reservoir models that are best described by 3 clusters. The updated model leads to a nearly 70% reduction in seismic data misfit. The final set of solutions successfully predict the observed normalized pressure history during the soak and flow-back into the wells between 82 and 175 days into the cyclic steaming operation.

INTRODUCTION

Time-lapse geophysical data, observations gathered from repeated geophysical surveys, are well suited for the monitoring of fluid flow within the Earth (Calvert 2005). As a result, time-lapse seismic data have been used to monitor the injection of carbon dioxide for underground storage (Arts et al. 2000), geothermal energy production, as well as to image fluid saturation and pressure changes in due to oil and gas production (e.g. Eastwood et al. 1994, Johnson et al. 1998, Tura and Lumley 1999, Landro et al. 2001, Behrens et al. 2002). The dynamic nature of time-lapse data, the fact that they are often related to saturation and fluid pressure changes, suggests that they could be used for aquifer and reservoir characterization, as noted in Landa and Horne (1997) and Vasco et al. (2004). The major impediment to successful characterization is the indirect relationship between the observations and the state of an aquifer or reservoir. To address this issue, a rock physics model is invoked to map the current state of the reservoir into seismic properties or attributes. This act introduces additional parameters that are necessary to characterize the poroelastic properties of the in-situ rock. These parameters are usually not well constrained, determined from a few cores or laboratory measurements. Furthermore, the properties almost always vary spatially, particularly between formations. Thus, the introduction of rock physics parameters presents yet another level of non-uniqueness (Chen and Dickens 2009). This is a barrier to aquifer and reservoir characterization that can be difficult to overcome.

As pointed out in Vasco et al. (2014, 2015) with sufficient temporal sampling it is possible to adopt an approach that mitigates some of the issues associated with the intervening rock physics model. In particular, it is possible to define onset times, the calendar time at which a geophysical quantity changes from its background value. Given a weak causality requirement, the onset time can often be related to the time at which saturation, fluid pressure, and temperature change within an aquifer or reservoir. Thus, the onset time is typically related to the arrival time of a fluid pressure and/or saturation front, and hence the to the propagation time of the fluid front, rather than the magnitude of such changes. As a result, onset times are sensitive to flow-related properties and relatively insensitive to the parameters of the rock physics model, as demonstrated in Vasco et al (2014, 2015).

In this paper we illustrate the utility of onset times by examining their use at a cyclic steam stimulation operation at the Peace River field (Figure 1) in Alberta, Canada (Lopez et al. 2015, Przybysz-Jarnut et al. 2016). This is a very complicated setting, with heterogeneity, prior production, and documented changes in pressure, temperature, and saturation. In fact, there were four periods of enhanced oil recovery at pad 31which covers the area that we will examine: a pad-wide cyclic steam injection from 2001 to 2011, a horizontal stream drive from 2012 until 2013, a pad-wide top-down steam stimulation starting in 2014 and extending beyond 2016, and a localized cyclic steam injection at just one well pattern (31-08) from August 2015 until February 2016. Fortunately, to aid in our analysis at pad 31 in the Peace River field there is a rich set of seismic monitoring data from a dense surface array (Figure 1). The array gathered daily seismic surveys to monitor the fluid-induced changes. The onset times allow for the compression of this multitude of seismic surveys into a single map of front propagation, which is used to image the heterogeneity within the reservoir.

METHODOLOGY

In this section we describe our approach for using repeat time-lapse geophysical observations, recorded by a permanently buried seismic system, to monitor fluid flow and to characterize the reservoir. The fact that the region has undergone previous production, necessitates a two-stage approach. First, we estimate the values of a set of global parameters, primarily describing the initial state of the reservoir and its large-scale permeability structure. Second, the finer scale permeability variations are determined from both reservoir production data and time-lapse observations of the travel times of seismic waves that propagate through the reservoir.

Governing Equations

Here we outline the equations governing the conditions within the reservoir and the changes due to fluid injection and production. Such changes lead to temporal and spatial variations in the seismic properties and we briefly mention Gassmann's (1951) approach for estimating elastic moduli in fluid saturated rock. Difficulties associated with estimating the fluid moduli lead us to the concept of the onset time of a change in a geophysical observable. We end this section with a brief description of the global and local updating schemes that will be used to estimate the reservoir properties.

Multiphase Flow and Thermal Stimulation

The reservoir operations at the Peace River field, involving cyclic steam stimulation to extract very viscous bitumen, are described and modeled using the equations of non-isothermal multi-component flow (Lopez et al. 2015, Przybysz-Jarnut et al. 2016). The multi-component mass and energy balance equations may be written succinctly using index notation (Pruess et al. 2011), where the index κ indicates one of the N_k fluid components and the $N_k + 1$ component signifies the heat that flows within the reservoir. The mass and energy balances are given by

$$\frac{\partial M^\kappa}{\partial t} = -\nabla \cdot \mathbf{F}^\kappa + q^\kappa \tag{1}$$

where M^κ is a mass accumulation term for the chemical component κ. The mass accumulation term is written in the form of a sum,

$$M^\kappa = \phi \sum_\beta S_\beta \rho_\beta X_\beta^\kappa \tag{2}$$

given in terms of the porosity ϕ, the saturation S_β, the density ρ_β, and the mass fraction X_β^κ of the fluid phase β. In the equation describing the energy balance the heat accumulation term for a multiphase system is given by

$$M^{N_k+1} = (1 - \phi)\rho_r C_r T + \phi \sum_\beta S_\beta \rho_\beta u_\beta \tag{3}$$

where ρ_r is the grain density of the rock, C_r is its specific heat, T is the temperature, and u_β is the specific internal energy in phase β. The advective flux vector for component κ, $\mathbf{F}^\kappa$, is a sum over all of the fluid phases, given by a multiphase form of Darcy's law,

$$\mathbf{F}^\kappa = \sum_\beta X_\beta^\kappa \mathbf{F}_\beta = \sum_\beta X_\beta^\kappa \rho_\beta \mathbf{w}_\beta = -k \sum_\beta X_\beta^\kappa \rho_\beta \frac{k_{r\beta}}{\mu_\beta} \left(\nabla P_\beta - \rho_\beta \mathbf{g} \right) \tag{4}$$

for a fluid phase traveling with the Darcy velocity $\mathbf{w}_\beta$. The absolute permeability k is a particularly important quantity, one of the main factors controlling fluid flow within the reservoir. The relative permeability $k_{r\beta}$ is usually determined from laboratory experiments on cores from the main formations of the reservoir. The fluid pressure for phase β, P_β, is one of the dependent variables along with the fluid saturation of the phase, S_β, and the temperature T. The fluid viscosity μ_β is determined from laboratory experiments on a given fluid at the appropriate temperatures and pressures of interest. Finally, $\mathbf{g} = g\mathbf{z}$ is the gravitational force vector that alters the flow in the presence of fluid density variations. The vector for the heat flux is given by

$$F^{N_k+1} = -\lambda \nabla T + \sum_\beta h_\beta \mathbf{F}_\beta \tag{5}$$

where λ is the thermal conductivity of the formation and h_β is the specific enthalpy in phase β. The quantities q^κ in equation (1) represent source or sink terms, often associated with injection or production wells.

In the forward problem we are given values for the aquifer or reservoir properties described by the parameters noted above, a reservoir model, and we solve the governing equations and accompanying equations-of-state, initial, and boundary conditions. The solution is usually constructed using a numerical fluid flow simulator (Peaceman 1977, Datta-Gupta and King 2007). For a realistic model solving the forward problem requires significant effort and is often computationally intensive because the governing equations are non-linear partial differential equations. Here, we shall tackle the inverse problem, in which we are given observations, both flow-related measurements and geophysical data, and tasked with estimating the characteristics of the aquifer or reservoir. This is typically a much greater challenge than the forward problem, requiring at least an order of magnitude more computation. Next, we develop a relationship

between time-varying fluid saturations, pressures, and temperatures within the Earth, and changes in the seismic properties at dep.

Relating Velocities and Elastic Moduli to Saturation, Temperature, and Pressure Changes

It is well known that fluid saturation, pressure, and temperature changes within and around an aquifer or reservoir will lead to changes in the elastic moduli of the fluid-filled porous medium and thus change its seismic characteristics. For example, the speed of a compressional wave transiting a saturated porous material, V_p, depends upon the saturated bulk modulus, K_{sat}, shear modulus, G_{fr}, and the density ρ_{sat} of the fluid filled rock according to (Mavko et al. 2009)

$$V_p = \sqrt{\frac{K_{sat} + \frac{4}{3}G_{fr}}{\rho_{sat}}} \tag{6}$$

We adopt Gassmann's equations (1951) to model the changes in elastic properties due to variations in fluid saturations, as they are generally accepted and widely used and found to agree with observations at seismic frequencies (Lumley 2001, Landro et al. 2001, Calvert 2005, Foster 2007). In Gassmann's approach the shear modulus is not influenced by the presence or absence of the fluid. Furthermore, the density of the fluid infiltrated rock is simply the weighted average of the component densities

$$\rho_{sat} = (1 - \phi)\rho_{solid} + \phi\rho_f \tag{7}$$

and for a multicomponent fluid the composite fluid density is given by the weighted sum

$$\rho_f = \sum_\beta S_\beta \rho_\beta \tag{8}$$

The bulk modulus of the fluid saturated rock has a more complicated dependence on the component properties, given by the function

$$K_{sat} = K_{fr} + \frac{\left(1 - K_{fr}/K_g\right)^2}{\phi/K_f + (1 - \phi)/K_g - K_{fr}/K_g^2} \tag{9}$$

where K_{fr} is the bulk modulus of the porous rock frame, ϕ is the effective porosity of the medium and the bulk modulus of the mineral K_g, which in the simplest case of a consolidated sandstone can be taken to be the bulk modulus of quartz. The parameter K_f is the bulk modulus of the pore-filling fluids

The original formulation of Gassmann only considered a single fluid saturating a porous rock. In order to generalize the approach, the fluid modulus, K_f, has been extended to cover the case in which the fluid is a mixture of several liquids and possibly gases. This leads to additional complications, with the essential difficulty that the composite modulus can depend upon how the fluids are distributed within the porous medium at length scales that are less than a seismic wavelength. By considering two extreme distributions one can derive upper and lower bounds on the effective fluid bulk modulus for a given fluid saturation, known as the Voigt and Reuss bounds, respectively (Mavko et al. 2009). In Figure 2 we plot the velocity variation based upon the Voigt and Reuss composite fluid moduli as a function of the water saturation, S_w. In a complex geologic setting, including oriented fracture systems, it can be difficult to determine which modulus is most representative. One compromise estimate involves taking the average of the two moduli, the so-called Hill average (Figure 2). Note that the differences in the calculated values of the three models shown in Figure 2 are almost as large as the entire variation due to the saturation change. We will

use these limiting moduli to illustrate variations in rock physics models and how they can impact calculated changes in seismic properties associated with changes in fluid saturations.

In addition, the cyclic steam stimulation process used at the Peace River field also produces coupled changes in pressure and temperature within the reservoir, leading to complicated rock physics models (Das and Batzle 2010, Kato et al. 2010). The model of Barker and Xue (2016) was used to map the saturation, temperature, and pressure changes into corresponding variations in elastic properties. The sensitivity of the seismic velocity variations as functions to gas and water saturations, pressure, and temperature are presented in Figure 3, showing the difficulty in interpreting velocity changes and hence seismic travel time and amplitude changes in terms of unique variations in saturation, pressure, and temperature within the reservoir. This difficulty is compounded by the fact that this area of the Peace River field has undergone earlier production, including a previous pad-wide cyclic steam stimulation that started in 2001and lasted until the end of 2011. The cyclic steam injection was followed by a brief implementation of a horizontal steam drive operation from 2012 to the end of 2013. These earlier production efforts resulted in spatially-varying temperatures, pressures, and saturations prior to the initiation of the top-down stream drive recovery process that ran from 2014 to the end of 2013, and the subsequent follow-up cyclic stream simulation on a single well pattern (31-08) that we shall analyze. The extreme heterogeneity in the initial conditions of the reservoir is indicated by the seismic amplitude variations in a regional time-lapse survey (Figure 4) used to diagnose well problems during the cyclic stream stimulation, conducted in March 2009. This legacy seismic reflection survey was conducted prior to the daily seismic monitoring that is the focus of our work. In Figure 4 one can observed large amplitude anomalies, associated with the appearance of gas that was expelled from the volatized oil as the pressure was reduced around the production wells, denoted by the black lines in the figure. Thus,

among other complexities, there are initial variations in gas saturation, temperature, and fluid pressures to contend with. This fact necessitates making these initial conditions a part of the inverse problem. That is, our inversion workflow will employ a global inversion approach as an initial step, in order to estimate the initial reservoir conditions and global properties.

The Onset of a Time-Lapse Change and its Relationship to Reservoir Dynamics

As noted above, the magnitudes of seismic velocity changes are influenced by the nature of the fluid distribution within the reservoir at length-scales that are less than the typical seismic wavelengths. Therefore, it can be difficult to relate changes in the magnitude of seismic velocities to changes in fluid saturation, pressure, and temperature in a quantitative sense. To overcome these problems, we use an onset time methodology to relate the time-lapse seismic data to the propagating fluid fronts. We will describe this approach using the Peace River reservoir monitoring program as an illustration (Lopez et al. 2015, Przybysz-Jarnut et al. 2015, 2016). A permanent seismic reservoir monitoring system was installed at the field consisting of 49 buried sources, in a rough grid with 200 to 220 m spacing, at a depth of 25 m (Figure 1). The 1492 receivers (hydrophones) are situated in a denser grid with 40 m spacing, in 20 m deep boreholes and packed in bentonite. The sources consisted of a set of 37.6 s long single frequency sweeps from 0.4 to 216 Hz. The entire set of 540 sweeps took 6 hours to complete for a single survey.

A time-lapse monitoring program was applied to a top-down steam drive oil recovery process that began in 2014, in which six new horizontal steam injection wells were drilled and operated above existing production wells drilled for an earlier cyclic stream stimulation (Lopez et al. 2015, Przybysz-Jarnut et al. 2016). The data are acquired in a continuous fashion and automatically

processed to generate four complete time-lapse data cubes every 24 hours (Lopez et al. 2015,

Przybysz-Jarnut et al. 2016). These four cubes are stacked to produce a single daily estimate. A

vertical time section through one such data cube is shown in Figure 5, along with a density log

from a well that is intersected by the cross-section. The pink curve is the top of the reservoir

(Bluesky formation) while the blue line indicates the base (Debolt formation). Small but visible

travel time shifts, for reflections from layers at the bottom of the reservoir, are evident in the two

snapshots plotted in Figure 6. The reservoir appears to be thicker than the dominant wavelength

of the seismic traces so tuning effects (Ghaderi and Landro 2009, Zhang and Castagna 2011),

which occur when the top and bottom reflections from the reservoir interfere, are probably not an

issue.

The daily monitoring allowed for the systematic extraction of small travel time and amplitude

changes for reservoir monitoring. Travel time shifts were extracted from the migrated time-lapse

cubes using a cross-correlation technique over a 120 ms window that extends beyond the bottom

of the reservoir. A triangular-weighting filter was applied to remove edge effects in the cross-

correlation estimates. An example of the time shifts generated by the top-down stream drive,

gathered between April 14, 2014 and March 30, 2015, are shown in Figure 7. There are clear

coherent anomalies within the area of interest, generally positive time shifts are co-located with

the overlying steam injection wells, and a large negative time shift anomaly is associated with the

production wells just south of the center of the well pad. In addition to the time shifts, we also

plot the time-lapse amplitude changes during this time interval. Note the small amplitude

decreases associated with the injection wells. However, there are much larger amplitude increases

that correlate with the large negative time shifts. These amplitude increases, and the negative time

shifts, are thought to be due to water from the condensed steam replacing gas that had been generated during the earlier cyclic steam injection. The areas containing this gas are indicated by amplitude anomalies in the legacy seismic survey from 2009 that is plotted in Figure 4. The time shifts associated with water encroaching on this region of accumulated gas are plotted in Figure 8, where we note the major contributing factors to the travel time shifts: fluid substitution, temperature, and fluid pressure changes.

The travel time shifts are sensitive to velocity changes and possibly deformation within the reservoir itself. In the manner of seismic tomography, the time shifts of waves propagating through the reservoir are a sum of the changes within each grid block of the reservoir model. Thus, if we consider a restricted segment of a seismic wave, propagating from a reference point just above the reservoir to the base of the reservoir, and then reflecting from the base of the reservoir and returning to the reference point, the total travel time shift is given by

$$T(x, y, \tau) - T_o(x, y) \tag{10}$$

$$= \sum_{n \in B(x,y)} \frac{L_n}{V_p(x, y, \tau, n)}$$

$$- \sum_{n \in B(x,y)} \frac{L_n}{V_o(x, y, n)}$$

where $B(x, y)$ denotes the indices of the grid blocks that are traversed by the seismic wave that is observed at location x, y of the seismic array, L_n is the propagation length within the specified grid block, and $V_p(x, y, \tau, n)$ is the seismic velocity within the grid block, $V_o(x, y, n)$ is the baseline velocity. For two surveys that are closely spaced in time we are assuming that the ray paths do not change significantly in equation (10). As noted above, the velocity is time-dependent due to the changes in fluid saturation, pressure, and temperature induced by the injection and production.

For our analysis of onset times we shall focus on an even later re-development on the southern-most portion of the production pad, where a single well set (31-08) underwent an additional cyclic steam stimulation (CSS). In this process steam was injected for 82 days, allowed to soak in and heat up the viscous oil, and then pumped out along with the mobilized oil. The normalized pressure response in the well, associated with one complete cycle which lasted for 175 days, is shown in Figure 9. The seismic data is translated into transit time shift maps, expressing the travel time changes for the seismic waves that propagate across the reservoir between a chosen baseline survey (e.g. the start of the cycle) and subsequent monitor surveys. Over the stimulation cycle shown in Figure 9, a total of 175 time lapse seismic surveys were available for integration (Figure 10). Note the temporal and spatial complexity of the time shifts around the two wells, as shown in Figure 10. The interpretation of the time shifts is based upon a rock physics model, using expressions (6), (9), and (10) for $T(x, y, \tau)$ given above, coupled with the relationship between the seismic velocity $V_p(x, y, \tau, n)$ and the changes in fluid saturation, pressure, and temperature provided by Gassmann's equation and the other rock physics expressions from Barker and Xue (2016) noted above.

As an illustration of the complex nature of the time shifts, consider the temporal variations in the size of the travel time shift at a location near the injection well 31-08 (Figure 11). Initially during the first 5 days the travel time shift increases slightly, possibly due to early fluid pressure increases, but after 15 days the travel time shift at this location has approached zero and turned negative after 15 days decreasing further over time. Such variations in sign are be expected, because saturation and pressure fronts propagate away from the injection well at substantially different velocities (Vasco 2011). Thus, pressure induced velocity changes can arrive at a location much faster than saturation changes. Similar considerations apply to thermal fronts which can

take even longer to move through a porous medium (Vasco 2010). Such transient fluid fronts are usually aliased by conventional time-lapse surveys, that are most often taken years apart, but they can be reliably imaged by a daily monitoring program. The fact that the magnitudes of the recorded time shift data combine processes involving pressure change, thermal effects, and saturation variations, makes it extremely challenging to incorporate them directly into a history matching procedure. For this reason, we utilize the onset time idea to integrate the seismic time shifts into a reservoir characterization scheme.

The onset time is defined as the calendar time at which the travel time shift exceeds a chosen threshold value. The first step is to define a threshold value that results in a meaningful definition of an onset time, as illustrated in Figure 11. This pre-defined threshold has two main roles: (1) to ensure that the magnitude of the seismic observation is above the background noise level (2) to define the physical process that is being tracked, which often decides the sign of the threshold value. Time-lapse seismic data are typically noisy due to non-repeatable environmental noise, source and sensor issues, and changes in near surface propagation due to variations in the water table or in the overlying water column. These variations lead to changes in the seismic characteristics even when there are no dynamic changes within the reservoir, thus we need a threshold value that distinguishes between the noise and a meaningful signal. Based upon the calculated signal-to-noise ratio for data from the array at Peace River, the threshold was defined as a time-shift decrease of 0.1 milli-seconds (Figure 11). To cross-validate the threshold value, we compared the signal with those from locations that are far from the well and where no changes are expected within the reservoir, as shown in Figure 12.

The use of onset times not only leads to a significant data reduction, collapsing the 175 daily time shift maps into a single spatial distribution of onset times, but has also been found to be less sensitive to the rock physics model used to interpret the seismic data (Vasco et al. 2014, 2015). As a demonstration of this, four different rock physics models were generated by linearly averaging the Reuss and Voigt estimates of the fluid modulus (Figures 2 and 3) to calculate the P-wave velocity. The variations of four such models with water saturation (S_w) are shown in Figure 3c, where we observe that the P-wave velocity is very sensitive to the method used to average the fluid moduli. In Figure 13, we plot the size of the time shift changes over the injection period (e.g. the first 82 surveys), calculated using the four models. In Figure 14 we generate the corresponding onset time maps for the four rock physics models. There are no noticeable differences between the calculated onset times (Figure 14) for the different models and all models display areal propagation of changes, related in this particular case to steam/fluid propagation. The similarity of the onset times stands in sharp contrast to the patterns of the magnitude of the travel time shifts which are strongly influenced by the particular rock physics model used for the calculations (Figure 13).

Inversion Strategy

Due to the coupled nature of our inverse problem, involving both fluid flow and seismic wave propagation, and the complicated processes and initial conditions, we adopt a two-stage inversion procedure that is outlined by the flow chart in Figure 15. Each step is illustrated by a panel in the figure. In the first step we conduct a sensitivity analysis in order to find the most important factor influencing our observations. A tornado diagram, such as the one in Figure 15, indicates those parameters that are the most influential by the length of each rectangle in the diagram. Second,

we implement an efficient parameterization for both the initial conditions and properties that is based upon an eigenvalue decomposition of the grid Laplacian matrix. Third, we determine both large-scale properties and initial conditions that are necessary for the fluid flow simulation and the calculation of the seismic time shifts using an evolution algorithm followed by a cluster analysis of the final population. In the last step we adjust the individual grid-block permeabilities in the reservoir model using an efficient tomographic-like approach to match the onset times. Because the focus of this paper is on matching the onset times, we discuss this step in some detail. Our description of the first steps of the inversion procedure is rather brief, with more details provided in Appendix A and Appendix B. Furthermore, an in-depth discussion of the inversion approach is also given in Hetz (2017) and in Hetz et al. (2017b).

Initial Determination of the Global Parameters

The coupled flow model contains a large number of parameters that need to be specified in order to conduct a numerical simulation. Some properties will be more important than others in controlling the simulation results. In order to discern those parameters that are to be included in the initial global inversion we conducted a sensitivity analysis as described in Hetz (2017). For the sensitivity study, the objective function was defined as the summation of misfits in the onset time seismic response, ΔOT_i, and the BHP

$$f(\mathbf{m}) = \sum_i^{Timestep} \left[\ln|\Delta OT|_i + \ln|\Delta BHP|_i \right] \tag{11}$$

By perturbing each parameter and examining the changes in the misfit we constructed a tornado diagram that indicates the relative importance of each major class of parameters in the misfit

functional. Based on the sensitivity analysis we found that all of parameters have some influence on the objective function, but the completion interval is the most important parameter indicating the need to adjust the size of stimulated zone. Other important parameters include the permeability and the initial gas saturation.

In order to successfully simulate fluid flow and seismic wave propagation in the reservoir, we need to specify the initial state of the reservoir, including the pressure, temperature, and saturation fields, and the large-scale properties of the model. A key element of this first step is a judicious representation of the fields in the initial model in order to maintain flexibility and prevent a proliferation of model parameters. In Appendix A we discuss a representation in terms of the eigenvectors of the Laplacian of the simulation grid (Bhark et al. 2011). That is, we represent the model $\mathbf{x}$ as a linear combination of M Laplacian eigenvectors $\mathbf{v}_i$

$$\mathbf{x} = \sum_{i=1}^{M} \phi_i \mathbf{v}_i \tag{12}$$

where ϕ_i are the weighting factors that are to be found in the inverse problem. This parameterization has the advantage that it is tied to the fluid flow simulation grid, which may be quite irregular in order to represent a complicated geological model. Furthermore, the representation provides a flexible parameterization that can describe a uniform model, a layered model, and a fully three-dimensional model, and all models in between these end-members. The lowest order basis functions are constants for each layer, while the second set of functions are composed of linear variations within the given layer. The higher order basis functions contain increasingly rapid spatial variations in properties. The weighted summation of the first ten basis functions gives the fields of initial properties.

The updating scheme for the global parameters is described in Appendix B. It is based upon the general notion of a set of Pareto optimal solutions (Lobato and Steffen 2017). We adopt this approach in order to treat the inverse problem as a multi-objective optimization task. That is, we are given two primary classes of observations, namely time-lapse seismic data and bottom hole pressure measurements, leading to two distinct misfit functions, given by (B1) and (B2) in Appendix B. We wish to determine models that minimize the misfit to the N_s observed onset times and N_b bottom hole pressures given by

$$M_s(\mathbf{x}) = \sqrt{\frac{1}{N_s}\sum_{i=1}^{N_s}(OT_i^o - OT_i^c)^2} \tag{12a}$$

and

$$M_b(\mathbf{x}) = \sqrt{\frac{1}{N_b}\sum_{i=1}^{N_b}(BP_i^o - BP_i^c)^2} \tag{12b}$$

respectively. To some degree the set of Pareto optimal solutions generalizes the notion of a trade-off curve in geophysical linear inverse theory (Menke 2018). In particular, Pareto optimal solutions cannot be improved with respect to a given objective function, such as the fit to the seismic onset times, without increasing the value of at least one of the other objective functions. As noted in Appendix B Pareto optimal solutions lie on the boundary of the set of feasible solutions, the Pareto front. We generate the set of feasible solutions using a stochastic evolutionary technique, the genetic algorithm (Park et al. 2015). In this approach we represent a model in terms of binary strings. A randomly generated collection of models progressively evolves from one generation to another by mutation (random changes) and recombination (joining of

portions of the models). The misfit functions $M_s(\mathbf{x})$ and $M_b(\mathbf{x})$ contribute to the definition of a

fitness function that is used to select the models that are retained in the succeeding generation.

The Pareto optimal solutions are defined with respect to the population of models in a generation.

This set of solutions is further sub-divided into groups of solutions using a clustering algorithm

[see Appendix B].

Local Updates of the Solution Clusters

The second major step in the inversion algorithm involves adjusting the clusters of solutions

through an iterative updating scheme. The entire process takes place on a fine-scale reservoir

model that may consist of tens of thousands to millions of grid blocks. Therefore, efficiency is a

paramount consideration. To this end we adopt a semi-analytic, streamline-based technique for

calculating model parameter sensitivities, first presented in Vasco et al. (2004). The general idea,

as it relates to the onset of changes in the time shifts, is that the injected fluids or transient pressure

fronts propagate outward from the source well to various points within the reservoir. For the cyclic

steam stimulation associated with the wells in the pattern 31-08 in the Peace River field we will

be concerned with injected steam, that may quickly condense into water, and associated pressure

and temperature changes.

The changes in the elastic moduli resulting from the arriving fluid fronts lead to changes in the

seismic waves propagating through the reservoir and alter the travel times of these waves. In the

absence of significant deformation, the onset of a change in the seismic travel time is directly

related to the arrival time of the fluid front. For a three-dimensional model we can compute

trajectories from each grid block where the saturation has changed to a point on the injection well

by streamline simulation (Datta-Gupta and King 2007). We can use time-of-flight methods to

relate the arrival or onset time to reservoir properties along the flow paths or streamlines (Vasco

et al. 1999, Vasco et al. 2005, Rey et al. 2012, Vasco and Datta-Gupta 2016, Watanabe et al. 2017).

As an illustration, consider the movement of a thermal front due to the injection of steam or hot

water along the streamline trajectories shown in Figure 16. The travel time for the injected steam,

after condensing to hot water, $\tau(\mathbf{r}_o, t)$, from a point on the injector, $\mathbf{r}_i$ to a location in the reservoir

where we observe a change in a geophysical observation, $\mathbf{r}_o$, is given by an integral along the flow

path

$$\tau(\mathbf{r}_o, t) = \int_{\mathbf{r}_i}^{\mathbf{r}_o} \frac{1}{|\mathbf{q}_w|} d\mathbf{r} \qquad (13)$$

where $\mathbf{q}_w(\mathbf{r}, t)$ is the velocity vector of the hot water at the leading edge of the coupled fluid front.

This vector follows from the form of the flux vector in equation (4) and is given by

$$\mathbf{q}_w(\mathbf{r}, t) = \frac{k}{\phi}(\kappa F_w' \nabla P - G_w \mathbf{z}), \qquad (14)$$

(Vasco and Datta-Gupta 2016) where

$$G_w = \frac{\frac{k_{rw} k_{rg}}{\mu_w \, \mu_g}}{\frac{k_{rw}}{\mu_w} + \frac{k_{rg}}{\mu_g} + \frac{k_{ro}}{\mu_o}} \left(\rho_w - \rho_g\right)g$$

and $\mathbf{z}$ is a unit vector pointing in the downward direction. The quantity $\kappa(S_w, S_g, S_o, P, T)$ is the

total fluid mobility given by

$$\kappa(S_w, S_g, S_o, P, T) = \frac{k_{rw}}{\mu_w} + \frac{k_{rg}}{\mu_g} + \frac{k_{ro}}{\mu_o}, \qquad (15)$$

that is usually considered to vary by formation but is most often taken as constant in a given

formation. Note that the total fluid mobility will depend upon the reservoir conditions, through its

dependence on the formation relative permeability curves and the fluid viscosities. The function $F_w'(S_w, S_g, S_o, P, T)$ is the derivative of the fraction flow curve for water

$$F_w(S_w, S_g, S_o, P, T) = \frac{\frac{k_{rw}}{\mu_w}}{\frac{k_{rw}}{\mu_w} + \frac{k_{rg}}{\mu_g} + \frac{k_{ro}}{\mu_o}} \tag{16}$$

(Peaceman 1977, Vasco and Datta-Gupta 2016) with respect to the water saturation S_w, which is also a function of the reservoir conditions and usually specified for each formation or lithology. The velocity of the thermal front is also a function of the porosity $\phi(\mathbf{r})$ and the absolute permeability $k(\mathbf{r})$. Finally, the front propagation is controlled by the pressure field that is established during the injection. As mentioned above, the transient behavior of the pressure field can be rapid in comparison to the propagation time of the saturation or thermal front. Therefore, we shall assume that, after the pressure transients have decayed, the average fluid pressure is primarily a function of spatial position $\mathbf{r}$ and will calculate it using a numerical reservoir simulator for a given initial or background reservoir model.

In each iterative step we seek local, or grid-block, updates to the permeability model that further refine the fits to the seismic onset times and the bottom hole pressure data. In computing model parameter sensitivities, we fix the relative permeability functions and the capillary pressure curves for the formation, using values obtained from the initial geological data and the global update, as well as the initial saturation, pressure, and temperature conditions of the reservoir and the large-scale porosity and permeability variations. The sensitivities, relating a perturbation in the permeability at a location in the reservoir to a deviation in the onset time are obtained from the path integral for saturation front travel time, $\tau(\mathbf{r}_o, t)$. That is, substituting the perturbed absolute permeability $k = k_o + \delta k$ into the expression for $\mathbf{q}_w(\mathbf{r}, t)$ and then into the integral gives

$$\delta\tau(\boldsymbol{r}_o, t) = \int_{r_i}^{r_o} \frac{1}{k_o|\boldsymbol{q}_o|} \delta k d\boldsymbol{r} \qquad (17)$$

where $\mathbf{q}_o$ signifies the fluid velocity in the background or current reservoir model. The semi-analytic expression for the sensitivity of the onset time is given by

$$\frac{\partial\tau}{\partial k} = \frac{1}{k_o|\mathbf{q}_o|} \qquad (18)$$

and provides the basis for an efficient, tomographic approach to refining the local permeability model using onset times (Vasco et al. 2014, 2015).

For each column of cells, the trajectory that represents the first arrival of the injected steam to a grid block in the column, is the path that determines the onset time for that location. Figure 16 shows the correlation between the time shift onset time and the saturation and the time-of-flight in days for a neutral tracer injected with the water. This travel time is proportional to the propagation time of the injected water. In order to map the time-of-flight of a neutral tracer to the travel time of the injected water we must multiply by the derivative of the fractional flow curve and the total mobility, as indicate above. The main purpose of Figure 16 is to illustrate the trajectories that are the basis for the semi-analytic sensitivities, given by equations (17) and (18), that for the basis for an efficient local inversion algorithm. Using a reservoir model, we may discretize the integral for the perturbed onset time associated with trajectory of the l-th streamline, τ_l, into a sum over the segment in each grid block of the reservoir model traversed by the path:

$$\delta\tau_l = \sum_{i \in \tau_l} \frac{1}{k_i|\mathbf{q}_i|} \delta k_i \qquad (19)$$

The set of paths to each point in the model where we have estimated an onset time leads to a system of equations, $\delta\boldsymbol{\tau} = \mathbf{M}\delta\mathbf{k}$, that may be solved in a least squares sense. That is, we minimize the sum of the squares of the residuals

$$R^2 = (\delta\boldsymbol{\tau} - \mathbf{M}\delta\mathbf{k})^t \cdot (\delta\boldsymbol{\tau} - \mathbf{M}\delta\mathbf{k}) \ . \tag{20}$$

The conditions for an extremum of R^2, the vanishing of the gradient with respect to the model parameters leads to the system of equations

$$\boldsymbol{M}^t \delta\boldsymbol{\tau} = \boldsymbol{M}\boldsymbol{M}^t \delta\boldsymbol{k} \tag{21}$$

that may be solved for $\delta\mathbf{k}$. The system of equations could be ill-posed if there are effectively fewer equations than unknowns. The usual remedy is to introduce additional regularization requirements, such as specifying that the magnitude of the model updates remains small if it is not constrained by the data, and, because the data cannot resolve small features, the spatial variations of the updates are often assumed to be smooth (Menke 2018). Such considerations, encapsulated in quadratic penalty terms lead to an augmented system of equations, as discussed in Vasco and Datta-Gupta (2016, p. 212). This matrix $\boldsymbol{M}$ is sparse because each trajectory only intersect a small percentage of the grid blocks in the model. Therefore, the system of equations (21) is solved using a least squares QR algorithm (LSQR) designed for large, sparse linear systems (Paige and Saunders 1982). In order to solve the nonlinear inverse problem, we iteratively update the model, adding perturbations and then recompute the residuals and quantities used in the linearized inversion, such as the saturation, pressure, and temperature fields. After a sufficient number of iterative updates, the misfit tends to level off, and the algorithm is terminated. In the section below, we illustrate the application of this approach to the data from the Peace River field.

APPLICATION TO TIME-LAPSE MONITORING AT PEACE RIVER

The methodology was applied to the southernmost region of pad-31 in the Peace River field, focusing on well set 31-08, three wells (31-8E1, 31-8E2, and 31-8W1) forming a 'tuning fork pattern' shown at the bottom of Figure 4. One positive feature of the area around pad-31 was that it lacked some of the vertical heterogeneity seen in other parts of the field. In particular, it did not contain shale baffles that had complicated the vertical flow in many other areas of the Peace River field.

Our analysis of the monitoring data from the Peace River field begins with the initial global history match in which we determine the initial, temperatures, pressures, and saturations as well as the large-scale variations in permeability and porosity. The inversion is based upon the initial portion of the cyclic steam stimulation involving the injection of hot steam, the first 82 days of the cycle. We use observations from the final soak and flow back to the well for validation purposes, attempting to predict the bottom hole pressure during this process using the history matched models. The initial water and gas saturations, porosity and permeability were taken from a geologic model provided by the operator, and the initial temperatures were obtained by interpolating the observed tubing head temperatures at the beginning of the cycle. The reservoir simulation model consisted of an irregular grid with 21 layers with variable boundaries.

The model representation of the global properties is in terms of the eigenvectors of the grid Laplacian matrix, the adjacency-based parameterization described above. A total of ten basis functions, eigenvectors of the Laplacian, were used in the representation of the porosity, permeability, initial water and gas saturations, and the initial temperature. The genetic algorithm

used to approximate the Pareto front and to determine the initial set of global parameters for the first step of our inversion scheme ran over 30 generations with population of 150 members per generation. The initial 150 models were generated stochastically by uniformly sampling from expected intervals of parameter values. The values of the model misfit functions associated with the seismic onset times, $M_s(\mathbf{x})$, and the reservoir bottom hole pressure data, $M_b(\mathbf{x})$, are plotted in Figure 17a. The initial scatter in the models, due to sampling randomly from the expected ranges of the parameters provides an indication of the variation in the two misfits expected in the model space for the range of all possible models. After 30 generations the genetic algorithm has reduced the misfit to both the seismic onset time observations and the bottom hole pressure data significantly in comparison to the prior cloud of solutions. The resulting suite of 150 models appear to define a tradeoff curve between the two misfit functions, the Pareto front. An application of the K-means cluster analysis algorithm generates three clusters that are color-coded in Figure 17b.

By applying a cluster analysis we further investigate the objective space. In particular, Figure 18 shows the updated onset time maps of selected models in cluster 1, cluster 2, and cluster 3, respectively. For all clusters, we observed some improvement from the initial onset time map calculated using the prior model. The improvements in the match to the bottom hole pressure data are shown in Figure 19, where we plot the calculated values for 40 models. One notable feature is the consistent pressure match during the soak validation interval, where we used the history matched models to predict the pressure behavior indicating that the models are able to adequately represent the saturation changes within the reservoir.

By looking at the parameter changes after the global update, as shown in Figure 20, we can gain some insight on the different physical mechanisms that are associated with the clusters. For

example, we observe that cluster 1 contains the greatest permeability decrease around the well. Also, the water saturation at the base of the reservoir increase more in cluster 1 as compared to clusters 2 and 3. This can explain the over-estimation of the well pressure associated with cluster 1 (Figure 19). Furthermore, the change in the temperature and gas saturation around the well in clusters 2 and 3 indicates different spatial flow patterns for these two models. These differences are reflected in the onset time maps as an underestimation of the propagation time.

The next stage of the inversion workflow involves adjustments to the reservoir permeabilities on the fine-scale grid in order to match the onset time observations for the first 82 days of steam injection and the bottom hole pressure. We apply the iterative linearized inversion algorithm to three candidate models which were selected based upon the cluster analysis. In Figure 21 we plot the normalized misfit as a function of the number of iterations of the algorithm. The misfit is reduced to almost 30% of its original value. Our iterative linearized algorithm is rather simple and uses a fixed step length for each iteration. The convergence is influenced by the weighting of the regularization and the characteristics of the linear solver that is applied at each step of the iteration. The updated onset time responses from the local step significantly improves the results due to the individual grid-block adjustments of reservoir flow properties. The changes made to permeability field, shown in Figure 22, reveal that models from both clusters share common characteristics with similar large-scale increases and decreases. These updates imply that the stimulated zones are located mostly around the vertical part of the well. Figure 23 displays the improvement in the pressure match and prediction as a result of the local updates for both clusters. Most notably, after the local update the excess pressures associated with first cluster from the global update are reduced to values much closer to the observed pressures (Figure 23a).

The final reservoir model produced by the inversion methodology is not only a useful tool for better matching the observations, but also gives additional insight into the state of the reservoir during the cyclic steaming operation. Figure 24, a plot the water saturation changes over the injection period, shows that the distribution of water is much less dispersed in the final clusters than it is in the initial model. The final models also help us to identify steam override during production, a common phenomenon in steam injection processes. The reason for this phenomenon is that mobility of displaced fluid is much lower than that of the displacing fluid (steam). Due to the differences in density between steam and the oil and water, steam override occurs. Figure 25 shows the water saturation along the streamlines over the injection period. At the beginning of the cycle (Figure25a) the steam starts moving upward as soon as it is injected inside the model. This movement is captured by the onset time map. The gravity override phenomenon becomes less severe over time, as the fluid starts to move downward at later times (Figure 25b). Overall our hierarchical history matching approach significantly reduces the misfit associated with the time-varying seismic and pressure data, and provides an improved representation of reservoir sweep through the identification of limits on the distribution of water and the detection of steam override.

DISCUSSION

The use of onset times should be viewed as the first step in the construction of a detailed reservoir model, whereby flow properties are obtained from geophysical time-lapse data. Because onset times are chiefly sensitive to the flow properties of a reservoir or aquifer, and much less sensitivity to the parameters of the rock physics model, they are well suited for estimating hydraulic conductivity or permeability. Furthermore, the onset times are related to the travel times

of fluid fronts, which have a quasi-linear relationship to properties such as hydraulic conductivity (He et al. 2006). As a result, inversions of onset times for properties such as permeability are much less sensitive to the initial or starting model, and less prone to become trapped in a local minimum, similar to seismic travel time tomographic imaging. The next step would be to use the magnitudes of the time shifts and reflection amplitudes to further refine the model and to estimate the poroelastic properties of the rock physics model. The final step would be to combine all of the data to construct the final reservoir model.

Like most surface seismic monitoring efforts our study was hampered by issues related to vertical resolution, due to the averaging of seismic waves and their dominantly vertical propagation. It may be possible to improve the resolution by including broadband data, larger offsets, and utilizing the full seismic waveform. Another option would be to use the pre-stack data directly for a tomographic estimation of the time shifts or the velocity changes. These enhancements should be topics for future research, as should be development of automated systems for seismic monitoring such as the continuous active seismic source monitoring system (Ajo-Franklin et al. 2011, Vasco et al. 2014). Such systems augment existing permanent arrays for monitoring reservoirs that exist in various fields around the world. While daily monitoring was possible at the Peace River field, the onset time approach is applicable to surveys that are separated by much longer intervals, such as yearly repeats (Vasco et al. 2015).

CONCLUSION

This study demonstrates the advantages of onset times, the recorded times at which a set of time-lapse geophysical data begin to deviate from their initial or background values, for high resolution reservoir characterization. A synthetic test shows that, in comparison to seismic time shift magnitudes, the onset times are insensitive to the details of the rock physics model used to relate the state of the reservoir to the seismic moduli. The methodology allows for the compression of multiple seismic surveys into a single map of onset times, that are directly related to fluid front propagation times. The compression of the frequent seismic surveys into a single set of onsets assists in the development of an efficient globally-convergent stochastic inversion technique, in this case the genetic algorithm.

The Peace River field case treated here displays all of the complexity that one encounters in enhanced oil recovery, including temperature and pressure variations, saturation changes, and complicated reservoir initial conditions. Using a hierarchical workflow, we were able to construct a set of initial models satisfying both the onset times and the well pressure data. The Pareto surface defines a set of feasible solutions, generalizing the concept of a trade-off curve used in linear inverse problems. Using local model updates, where the flow properties were adjusted on a cell-by-cell basis, the algorithm was able to improve upon the global stochastic solution. The final set of reservoir models not only match the data used in the inversion, they also successfully predict well pressure data set aside for validation. Finally, the reservoir models provide insight into the processes operating in the reservoir during the cyclic steaming operation. In particular, the models predict a much sharper water/steam front and reveal steam override due to the influence of gravity.

Finally, the estimates of the initial conditions and local permeabilities, allowed us to construct an improved injectivity profile along the horizontal well, which is crucial for further development considerations.

ACKNOWLEDGMENTS

REFERENCES

Ajo-Franklin, J., Daley, T., Butler-Veytia, T., Peterson, J., Wu, Y., Kelly, B., and Hubbard, S. 2011. Multi-level continuous active source seismic monitoring (ML-CASSM): mapping shallow hydrogracture evolution at a TCE contamination site, SEG Expanded Abstracts, 30, 3727.

Arenas, E., van Kruijsdijk, C., and Oldenziel, T. 2001. Semi-Automatic History Matching Using the Pilot Point Method Including Time-Lapse Seismic Data. In *SPE Annual Technical Conference and Exhibition*: Society of Petroleum Engineers.ISBN 1555631541.

Arts, R., Brevik, I., Eiken, O. et al. 2000. Geophysical Methods for Monitoring Marine Aquifer Co2 Storage–Sleipner Experiences. In *5 th International Conference on Greenhouse Gas Control Technologies, Cairns, Australia*.

Barker, T. and Xue, Y. 2016. Inversion of Continuous 4D Seismic Attributes to Reveal Daily Reservoir Changes. In *SEG Technical Program Expanded Abstracts 2016, p. 5527-5531*, Society of Exploration Geophysicists.

Behrens, R., Condon, P., Haworth, W. et al. 2002. 4D Seismic Monitoring of Water Influx at Bay Marchand: The Practical Use of 4d in an Imperfect World. *SPE Reservoir Evaluation & Engineering* **5** (5): 410-420. DOI: 10.2118/79961-PA

Bhark, E.W., Jafarpour, B., and Datta-Gupta, A. 2011. A Generalized Grid Connectivity-Based Parameterization for Subsurface Flow Model Calibration. *Water Resources Research* **47**. DOI: Artn W0651710.1029/2010wr009982

Calvert, R. 2005. *Insights and Methods for 4D Reservoir Monitoring and Characterization*, EAGE/SEG Distinguished Instructor Short Course, No. **8**, Society of Exploration Geophysicists, Tulsa

Chen, J. and Dickens, T. A. 2009. Effects of uncertainty in rock-physics models on reservoir parameter estimation using seismic amplitude variation with angle and controlled-source electromagnetics data, *Geophysical Prospecting*, **57**, 51-74, doi: 10.1111/j.1365-2478.2008.00721.x

Dadashpour, M., Ciaurri, D.E., Mukerji, T. et al. 2010. A Derivative-Free Approach for the Estimation of Porosity and Permeability Using Time-Lapse Seismic and Production Data. *Journal of Geophysics and Engineering* **7** (4): 351-368. DOI: 10.1088/1742-2132/7/4/002

Dadashpour, M., Echeverría-Ciaurri, D., Kleppe, J. et al. 2009. Porosity and Permeability Estimation by Integration of Production and Time-Lapse near and Far Offset Seismic Data. *Journal of Geophysics and Engineering* **6** (4): 325.

Dadashpour, M., Landro, M., and Kleppe, J. 2008. Nonlinear Inversion for Estimating Reservoir Parameters from Time-Lapse Seismic Data. *Journal of Geophysics and Engineering* **5** (1): 54-66. DOI: 10.1088/1742-2132/5/1/006

Das, A., and Batzle, M. 2010. Modeling studies of heavy oil-In between solid and fluid properties, in *Heavy Oils: Reservoir Characterization and Production Monitoring*, S. Chopra, L. R. Lines, D. R. Schmitt, and M. L. Batzle (Eds), Society of Exploration Geophysicists, Tulsa.

Das, I. and Dennis, J. E. 1998. Normal-boundary intersections: A new method for generating the Pareto surface in nonlinear multicriteria optimization problems, *SIAM Journal on Optimization*, **8**, 631, doi: 10.1137/S1052623496307510.

Datta-Gupta, A. and King, M. 2007. *Streamline Simulation: Theory and Practice*: Society of Petroleum Engineers. Original edition. ISBN.

Deb, K. 2001. *Multi-Objective Optimization using Evolutionary Algorithms,* John Wiley and Sons, New York.

Deb, K., Pratap, A., Agarwal, S., and Meyarivan, T. 2002. A fast and elitist multiobjective genetic algorithm: NSGA-II, *IEEE Transactions of Evolutionary Computation*, **6**, 182-197.

Eastwood, J., Lebel, P., Dilay, A. et al. 1994. Seismic Monitoring of Steam-Based Recovery of Bitumen. *The Leading Edge* **13** (4): 242-251.

Erfani, T., and Utyuzhnikov, S. V. 2011. Directed search domain: A method for even generation of Pareto frontier in multiobjective optimation, *Journal of Engineering Optimization*, **43**, 1-18.

Foster, D.G. 2007. The BP 4-D Story: Experience over the Last 10 Years and Current Trends. In *International Petroleum Technology Conference*: International Petroleum Technology Conference.ISBN 1555631843.

Gassmann, F. 1951. Elastic Waves through a Packing of Spheres. *Geophysics* **16** (4): 673-685. DOI: 10.1190/1.1437718

Ghaderi, A., and Landro, M. 2009. Estimation of thickness and velocity changes of injected carbon dioxide layers from prestack time-lapse seismic data, *Geophysics*, **74**, O17-O28.

He, Z., Yoon, S., and Datta-Gupta, A. 2002. Streamline-Based Production Data Integration with Gravity and Changing Field Conditions. *SPE Journal* **7** (4): 423-436.

He, Z., Datta-Gupta, A., Al-Harbi, M., and Vasco, D. W. 2006. Rapid inverse modeling of pressure interference tests using trajectory-based travel time and amplitude matching, *Water Resources Research*, **42**, W03419, 1-15.

Hetz, G. 2017. Ph. D. thesis, Texas A & M University.

Hetz, G., Datta-Gupta, A., Przybysz-Jarnut, J. et al. 2017a. Integration of Continuous Time Lapse Seismic Data into Reservoir Models Using Onset Times. In *First EAGE Workshop on Practical Reservoir Monitoring*.ISBN 2214-4609.

Hetz, G., Kim, H., Datta-Gupta, A., King, M. J., Przybysz-Jarnut, J. K., Lopez, J. L., and Vasco, D. W. 2017b. History matching of frequent seismic surveys using seismic onset times at the Peace River field, Canada, Paper 187310 presented at the SPE Annual Technical Conference and Exhibition, San Antonio, Texas, 7-12 October.

Jafarpour, B., and McLaughlin, D. B. 2009. Reservoir characterization with the discrete cosine transform, *SPE Journal*, **14** (1), 182-201.

James, G., Witten, D., Hastie, T., and Tibshirani, R. 2017. *An Introduction to Statistical Learning*, Springer, New York.

Johnson, D. H., McKenny, R. S., Verbeek, J., and Almond, J., 1998. Time-lapse seismic analysis of Fulmar field, *The Leading Edge*, **17**, 1420-1428.

Kato, A., Onozuka, S., and Nakayama, T. 2010. Elastic property changes in a bitumen reservoir during steam injection, in *Heavy Oils: Reservoir Characterization and Production Monitoring*, S. Chopra, L. R. Lines, D. R. Schmitt, and M. L. Batzle (Eds), Society of Exploration Geophysicists, Tulsa.

Kennett, B. 1983. *Seismic Wave Propagation in Stratified Media*: Cambridge University Press Original edition. ISBN 0521239338.

Landa, J. L., and Horne, R. N., 1997. A procedure to integrate well test data, reservoir

performance history, and 4-D seismic information into a reservoir descriptio, Paper SPE 38653 presented at the 1997 Annual Technical Conference, Society of Petroleum Engineers.

Landrø, M., Digranes, P., and Strønen, L. 2001. Mapping Reservoir Pressure and Saturation Changes Using Seismic Methods-Possibilities and Limitations. *First break* **19** (12): 671-684.

Lobato, F. S., and Steffen, V. 2017. *Multi-Objective Optimization Problems - Concepts and Self-Adaptive Parameters with Mathematical and Engineering Aplications*, Springer, Cham, Switzerland

Lopez, J., Wills, P., La Follett, J. et al. 2015. Real-Time Seismic Surveillance of Thermal Eor at Peace River. In *SPE Canada Heavy Oil Technical Conference*: Society of Petroleum Engineers.ISBN 1613994028.

Lumley, D.E. 2001. Time-Lapse Seismic Reservoir Monitoring. *Geophysics* **66** (1): 50-53. DOI: 10.1190/1.1444921

Mavko, G., Mukerji, T., and Dvorkin, J. 2009. *The Rock Physics Handbook: Tools for Seismic Analysis of Porous Media*: Cambridge university press. Original edition. ISBN 0521861365.

Menke, W. 2018. *Geophysical Data Analysis: Discrete Inverse Theory*, Academic Press, London.

Messac, A., and Mattson, C. A. 2004. Normal constraint method with guarantee of even representation of complete Pareto frontier, *AIAA Journal*, **42**, 2101-2111.

Mindlin, R. 1949. Compliance of Elastic Bodies in Contact. *J. of Appl. Mech.* **16**.

Mindlin, R.D. 1949. Compliance of Elastic Bodies in Contact. *Journal of Applied Mechanics* **16**: 259-268.

Paige, C.C. and Saunders, M.A. 1982. Lsqr: An Algorithm for Sparse Linear Equations and Sparse Least Squares. *ACM transactions on Mathematical Software* **8** (1): 43-71.

Park, H.-Y., Datta-Gupta, A., and King, M. 2013. Handling Conflicting Multiple Objectives Using Pareto-Based Evolutionary Algorithm for History Matching of Reservoir Performance. Paper SPE 163623 presented at the SPE Reservoir Simulation Symposium, The Woodlands, Texas, USA, 163618-163620 February.

Park, H.-Y., Datta-Gupta, A., and King, M.J. 2015. Handling Conflicting Multiple Objectives Using Pareto-Based Evolutionary Algorithm During History Matching of Reservoir Performance. *Journal of Petroleum Science and Engineering* **125**: 48-66.

Peaceman, D. W. 1977. *Fundamentals of Numerical Reservoir Simulation*, Elsevier Scientific Publishing, Amsterdam

Pruess, K., Oldenburg, C., and Moridis, G. 2011. *Tough2 Users Guide, Version 2*, Earth Sciences Division, Lawrence Berkeley Laboratory, Berkeley.

Przybysz-Jarnut, J., Didraga, C., Potters, J. et al. 2015. Value of Information of Frequent Time-Lapse Seismic for Thermal Eor Monitoring at Peace River. In *SPE Annual Technical Conference and Exhibition*: Society of Petroleum Engineers.ISBN 1613993765.

Przybysz-Jarnut, J., Wills, P., Araujo, M. et al. 2016. Combining Frequent 4d Seismic and Mechanistic Reservoir Modeling to Improve the Effectiveness of Steam Injection Operations. In *SPE Annual Technical Conference and Exhibition*: Society of Petroleum Engineers.ISBN 161399463X.

Rey, A., Bhark, E., Gao, K. et al. 2012. Streamline-Based Integration of Time-Lapse Seismic and Production Data into Petroleum Reservoir Models. *Geophysics* **77** (6): M73-M87. DOI:

10.1190/Geo2011-0346.1

Shell Canada 2016. *Peace River In-Situ Oil Sands Progress Report*.
https://www.aer.ca/documents/oilsands/insitu-
presentations/2016PeaceRiverShellPeaceRiverSAGD8143.pdf

Taubin, G. 1995. A signal processing approach to fair surface design, paper presented at
SIGGRAPH 1995, Association for Comput. Mach. Spec Interest Group on Computer
Graphics and Interactive Technology, Los Angeles, California.

Tura, A. and Lumey, D.E. 1999. Estimating Pressure and Saturation Changes Time-Lapse Avo
Data. In *SEG Technical Program Expanded Abstracts 1999*: Society of Exploration
Geophysicists.

Vasco, D. W. 2010. Fluid flow in a heterogeneous medium under nonisothermal conditions,
Water Resource Research, **46**, doi:10.1029/2010WR009571.

Vasco, D. W. 2011. On the propagation of a coupled saturation and pressure front, *Water
Resources Research*, **47**, doi: 10.1029/2010WR009740.

Vasco, D.W. and Datta-Gupta, A. 2016. *Subsurface Fluid Flow and Imaging,* Cambridge
University Press. Original edition. ISBN 1316577945.

Vasco, D.W., Bakulin, A., Baek, H., and Johnson, L. R. 2015. Reservoir Characterization Based
Upon the Onset of Time-Lapse Amplitude Changes. *Geophysics* **80** (1): M1-M14. DOI:
10.1190/Geo2014-0076.1

Vasco, D.W., Daley, T.M., and Bakulin, A. 2014. Utilizing the Onset of Time-Lapse Changes: A
Robust Basis for Reservoir Monitoring and Characterization. *Geophysical Journal
International* **197** (1): 542-556. DOI: 10.1093/gji/ggt526

Vasco, D.W., Datta-Gupta, A., Behrens, R. et al. 2004. Seismic imaging of reservoir flow
properties: Time-lapse amplitude changes, *Geophysics*, **69**, 1425-1442.

Vasco, D.W., Yoon, S., and Datta-Gupta, A. 1999. Integrating Dynamic Data into High-
Resolution Reservoir Models Using Streamline-Based Analytic Sensitivity Coefficients.
SPE Journal **4** (4): 389-399. DOI: Doi 10.2118/59253-Pa

Watanabe, S., Han, J., Hetz, G. et al. 2017. Streamline-Based Time-Lapse-Seismic-Data
Integration Incorporating Pressure and Saturation Effects. *SPEJ Society of Petroleum
Engineers*., 166395-PA, doi.org/10.2118/166395-PA

Zhang, R., and Castagna, J. 2011. Seismic sparse-layer reflectivity inversion using basis pursuit
decomposition, *Geophysics*, **76**, R147-R158, doi:10.1190/geo2011-0103.1.

Appendix A: Model Representation

Because the inversion approach contains what we are calling global and local model updates, essentially large-scale and fine-scale spatial variations of in the properties of the model, we need a flexible model representation that allows for a seamless transition between spatial scales. In this Appendix we briefly describe one such parameterization, as we will incorporate it into our two stage inversion scheme. We shall define the grid by its set of vertices V and edges E, characterizing it by a graph $G=(V,E)$. The N vertices, $V=\{1,2,...,N\}$, represent the center of the grid cells at which the reservoir properties are defined. The edges E represent connections between vertices and one can specify the set of edges using an adjacency matrix a_{ij}, where the non-zero entries denote a connection between vertices v_i and v_j. Specifically, the entries of the $N \times N$ grid adjacency matrix $\mathbf{A}$ are given by

$$a_{i,j} = \begin{cases} 1 & (i,j) \in E \\ 0 & (i,j) \notin E \end{cases} \tag{A1}$$

because we are only considering unweighted connections between vertices. Jafarpour and McLaughlin (2009) showed that a low dimensional approximation may be given by the lowest frequency Fourier components. In order to extend this approach to an irregular mesh we make use of the association, first noted by Taubin (1995), between the discrete Fourier transform of a function and the decomposition of the function into a linear combination of the eigenvectors of the Laplacian of the grid. The grid Laplacian is a discrete second-order differencing operator given by

$$\mathbf{L}_{ij} = \begin{cases} d_i & i = j \\ -1 & (i,j) \in E \\ 0 & otherwise \end{cases} \tag{A2}$$

where d_i is the degree of the i-th vertex

$$d_i = \sum_{j=1}^{n} a_{ij} \tag{A3}$$

a measure of the number of edges connected to the vertex. The Laplacian provides a measure of the connectivity of the grid and for many commonly encountered boundary conditions the discrete operator is a positive semi-definite, symmetric matrix (Bhark et al. 2011). Given these properties we may use the spectral theorem to construct an eigen-decomposition of the Laplacian matrix

$$\mathbf{L} = \mathbf{V}\mathbf{\Lambda}\mathbf{V}^{\mathrm{T}} = \sum_{i=1}^{N} \lambda_i \mathbf{v}_i \, \mathbf{v}_i^{T} \tag{A4}$$

where the vectors $\mathbf{v}_i$ are pairwise orthogonal unit eigenvectors. The eigenvalues λ_i are the modal frequencies associated with the Laplacian eigenvectors, a direct consequence of the equivalence between the Laplacian eigenvectors and the basis set of the discrete Fourier transform (Taubin 1995). Here, we will represent the model $\mathbf{x}$ as a linear combination of basis vectors that consist of the Laplacian eigenvectors

$$\mathbf{x} = \sum_{i=1}^{M} \phi_i \mathbf{v}_i \tag{A5}$$

where M is small for a large-scale global specification of properties and equal to N for a full-scale representation of the model. This representation is referred to as an adjacency-based transformation or parameterization. The low frequencies, or small values of M, can be used to represent the global properties of the model, such as a uniform layer velocity, while the highest frequencies account for much more rapid local variations in properties. By changing the value of M used in our representation we can switch between inversions for local and global properties.

Appendix B: Determination of the Global Parameters

In this Appendix we describe our approach for determining the global properties of the model, including the initial saturations, pressure, and temperature of the reservoir, as well as the large-scale porosity and permeability values at the beginning of the stimulation cycle. As a first step, a sensitivity analysis is conducted in order to identify the parameters to be considered in the global updating scheme. A description of that effort is presented in Hetz et al. (2017) and Hetz (2017) and will not be repeated here. We consider the calibration or inversion procedure to be a multi-objective optimization problem. There are two classes of observations, geophysical measurements and hydrological or reservoir engineering data, that need to be matched. Each set may be used to generate a misfit functional by considering the sum of the square of the residuals. That is, we consider the collection of onset times constructed from the seismic time lapse observations, giving the misfit functional associated with the reservoir model $\mathbf{x}$

$$M_s(\mathbf{x}) = \sqrt{\frac{1}{N_s}\sum_{i=1}^{N_s}(OT_i^o - OT_i^c)^2} \qquad \text{(B1)}$$

measuring the difference between the observed onset time OT_i^o and the calculated onset time OT_i^c, and the bottom hole pressure measurements

$$M_b(\mathbf{x}) = \sqrt{\frac{1}{N_b}\sum_{i=1}^{N_b}(BP_i^o - BP_i^c)^2} \qquad \text{(B2)}$$

where BP_i^o are the observed bottom hole pressure and BP_i^c are the calculated bottom hole pressures for the i-th observation point. We can linearly combine the misfit functionals to produce a composite measure of sum of the squared residuals. However, it can be a challenge to correctly weight the two classes of data in order to produce a meaningful model. The conventional approach

in geophysics is to construct a trade-off curve through a series of inversions, and to pick a point that balances the fits to each data class (Menke 2018). While this technique is useful linear inverse problems, it can encounter difficulties for nonlinear inverse problems, such as our inversion for reservoir properties.

One alternative to the minimization of a composite misfit is to consider multi-objective optimization techniques characterizing the trade-off between different objective functions. A general approach is provided by the notion of Pareto optimal solutions (Lobato and Steffen 2017). These are solutions that cannot be improved with respect to any particular objective function without degrading at least one of the other objective functions. To describe such solutions, consider a multi-objective optimization problem formulated as the minimization of a vector of m objective functions

$$\min_{\mathbf{x} \in \mathbf{X}} \mathbf{M}(\mathbf{x}) = [M_1(\mathbf{x}), M_2(\mathbf{x}), \dots, M_m(\mathbf{x})] \tag{B3}$$

where $\mathbf{X}$ is the set of feasible solutions. One may also characterize Pareto optimal models using the notion of solution dominance. A feasible solution $\mathbf{x}_1$ is said to Pareto dominate another feasible solution $\mathbf{x}_2$ if

$$M_i(\mathbf{x}_1) \leq M_i(\mathbf{x}_2) \tag{B4}$$

for all indices $i \in \{1, 2, \dots, m\}$ and

$$M_j(\mathbf{x}_1) < M_j(\mathbf{x}_2) \tag{B5}$$

for at least one index $j \in \{1, 2, \dots, m\}$. A solution is called Pareto optimal if there does not exist another solution that dominates it. The set of optimal solutions constitutes the Pareto front or boundary and characterize the trade-off between the various objective functions.

A class of stochastically driven techniques, known as evolutionary algorithms, provide an a means of generating a Pareto front (Deb 2001). The genetic algorithm, perhaps the most widely used of these techniques, was motivated by an analogy with biological evolution. In particular, an initial set of models is constructed using a random number generator. The parameters describing each model are converted to binary strings, the full description of each model is referred to as a genome or chromosome. The family of models is successively updated by recombination and mutation. Recombination involves taking selected pairs of individuals and forming new members by randomly combining various segments from the two models. The new model will thus be a hybrid model with characteristics of both parent models. In addition, the process of mutation introduces random changes into the genomes of some subset of the new models. The evolution of the population of models is governed by a fitness function of the form $\exp[-f(\mathbf{x}_i)]$ where $f(\mathbf{x}_i)$ is the objective function. That is, the probability of selecting a particular model to take part in the construction of the next generation is given by a function of the general form

$$P(\mathbf{x}_n) = \frac{\exp[-f(\mathbf{x}_n)]}{\sum_i \exp[-f(\mathbf{x}_i)]} \tag{B6}$$

once a new generation of models is produced it is used in the next iteration of the algorithm. The process is repeated until the overall fitness of the population reaches a satisfactory level of some maximum number of generations has been produced.

One issue associated with this approach is that it can fail to adequately define non-convex Pareto fronts such as those associated with non-linear inverse problems. We use a stochastically driven technique to address this problem by:

    i)   Assigning fitness to population members based on non-dominated sorting and ranking.

ii) Preserving diversity among solutions on the same front by examining the distance between solutions (Deb et al. 2002). The models are first sorted according to their dominance rank (Figure 10).

That is, solutions that are not dominated by any other models with respect to the given objective functions, those lying on or closest to the Pareto front are considered Rank 1 or belonging to Front 1. A model of Rank 2, or lying in Front 2, is only dominated by those of Rank 1 and no others. Generally, a model in Front k+1: (1) Should be dominated by at least one model in Front k; (2) May or may not dominate solutions in Front k+2 (Park et al. 2013).

Rather than use the expression $P(\mathbf{x}_n)$ given above, the fitness is equal to the rank of the model. If two models have equal rank than the model with the larger crowding distance [$cdist^i$ in Figure B1] is selected to take part in the construction of the next generation through cross-over and mutation.

Finally, the distance between solutions is used to define clusters of solutions that share similar characteristics. This is accomplished using a standard approach, the K-means clustering algorithm (James et al. 2017, p. 386). We start by assuming that the solutions may be grouped in some number, say *K,* of clusters. This number may change as we try to find the optimal set of clusters. The main goal is to partition the dataset into internally homogeneous and externally distinct groups. The idea is to minimize the within-cluster different between solutions, $W(C_k)$, usually defined by the sum of the square of the distance between each solution in cluster *k*.

$$W(C_k) = \frac{1}{|C_k|}\sum_{i \in C_k}|\mathbf{x}_i - \overline{\mathbf{x}_k}|^2 \tag{B7}$$

where $\overline{\mathbf{x}_k}$ is the cluster centroid and $|C_k|$ denotes the number of solutions in cluster *k*. The approach is initialized by randomly assigning solutions to one of the clusters and computing the centroid of the *K* clusters. Then the following steps are repeated until the within-cluster distances

and cluster assignments stop changing: (1) Reassign the observations to the centroid which lies closest to that solution (2) After the reassignment, recompute the cluster centroids. This approach is guaranteed to decrease the measure of total within-cluster distances

$$W_{total} = \sum_k W(C_k) \tag{B8}$$

as explained in James et al. (2017, p. 402). The clusters provide an initial set of solutions which we can update in order to match the seismic onset times and bottom hole pressure observations, as described next.

Figures:
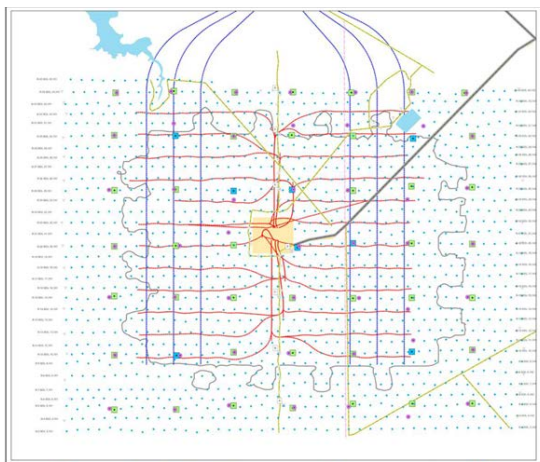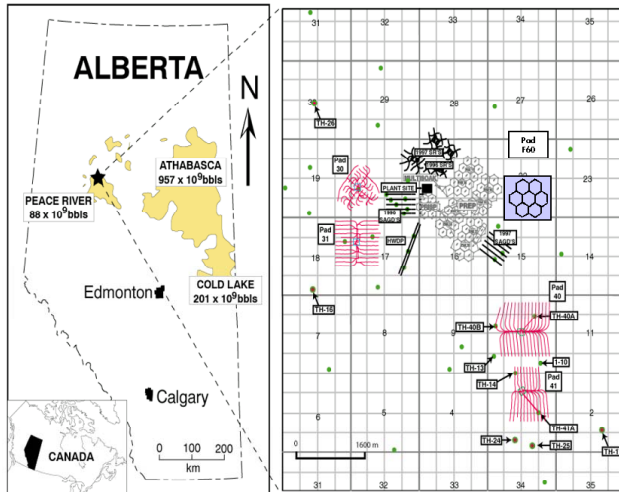
Figure 1. (Top) Map showing the location of the Peace River field in Alberta Canada. The location of Pad 31 is indicated by the schematic diagram on the right, along with other well pads. The area of the map on the right is 9500m by 8000m. (Bottom) Pad 31 horizontal production wells (red) and injection wells (blue). The area covered by the production wells is 1.5 km by 1.5 km in the north-south and east-west directions, respectively. Also shown are seismic sources (green squares) and receivers (blue dots). Pad 31 first underwent cyclic steam stimulation (CSS) in 2001 and then top-down steam drive using the configuration of wells shown in this figure, and is the focus of this study. Map modified from Shell Canada (2016).

.
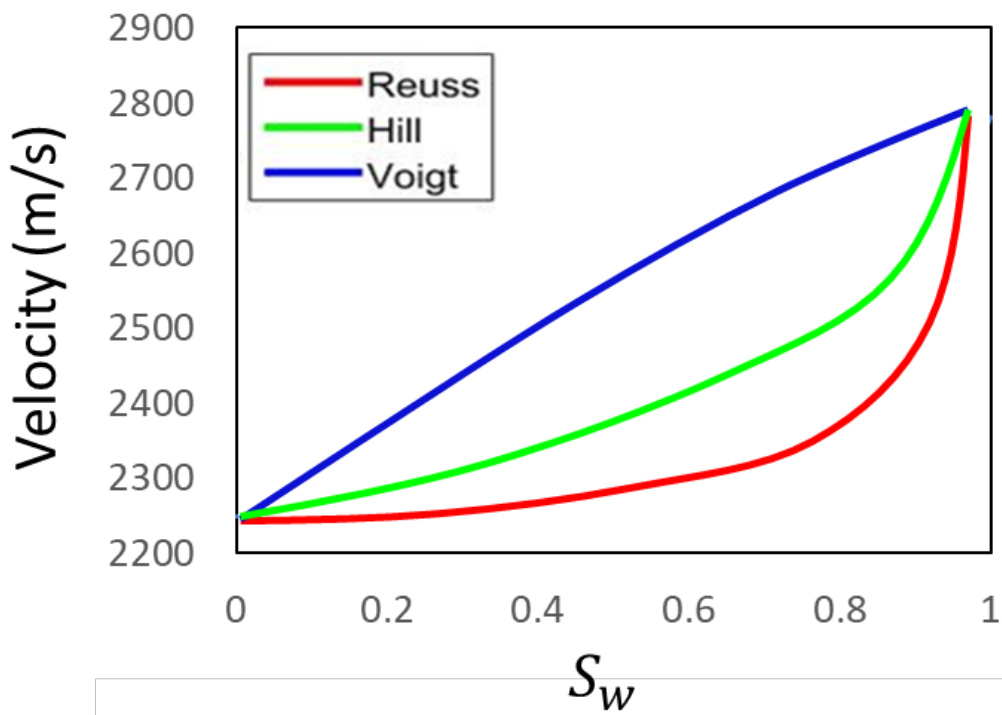
Figure 2. Compressional wave velocity as a function of water saturation, based upon the Reuss, Hill, and Voigt composite moduli.
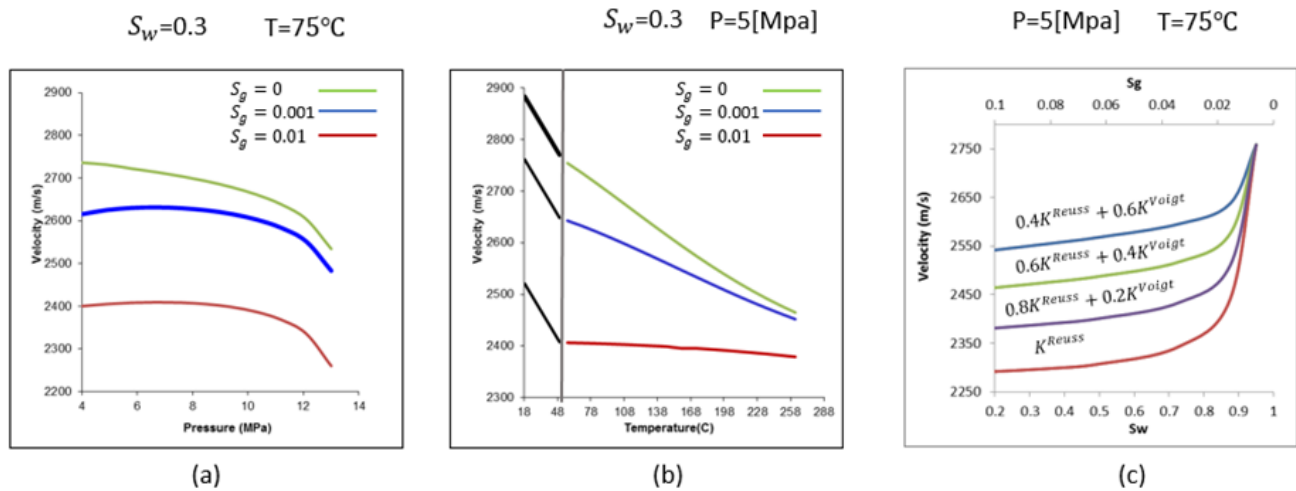
Figure 3.   Sensitivity of the rock physics model. (a) Velocity of a compressional wave as a function of pressure for different gas saturation where temperature and water saturation are fixed. (b) Velocity of a compressional wave as a function of temperature for different gas saturation where pressure and water saturation are fixed. The vertical black line denotes a transition temperature from one equation-of-state to another. At temperatures less than 48 degrees the model depends upon a correlation, as discussed in Barker and Xue (2016). (c) Velocity of a compressional wave as a function of the saturations. All velocity estimates are computed by Gassmann's approach but using four different methods for calculating the composite fluid bulk modulus
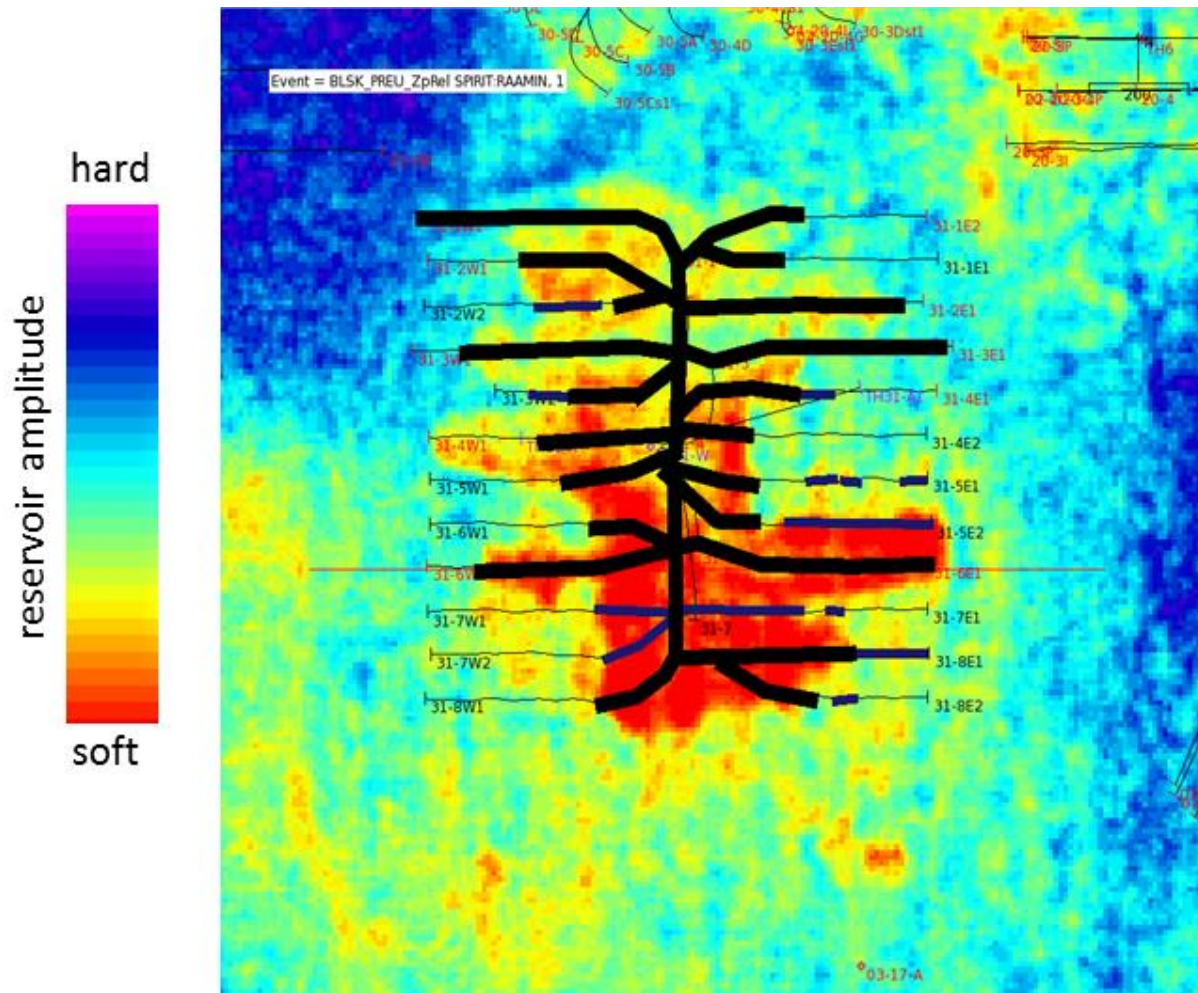
Figure 4. Seismic root-mean-squared (RMS) amplitudes gathered in March 2009 after earlier cyclic steam operation at Peace River. Warm colors (red/yellow/green) represent high RMS amplitudes due to thermal stimulation, likely due to the appearance of gas after pressure was reduced due to production. The producing wells associated with the current top-down steam drive are indicated by black lines and covers a 1.5 by 1.5 km area. The thickened portions of the black lines indicate where the well is thought to be open. Cyclic steam stimulation at this pad began in 2001 and was followed by top-down steam drive in 2014. Figure modified from Lopez et al. (2015).

Track number (increasing to the east)
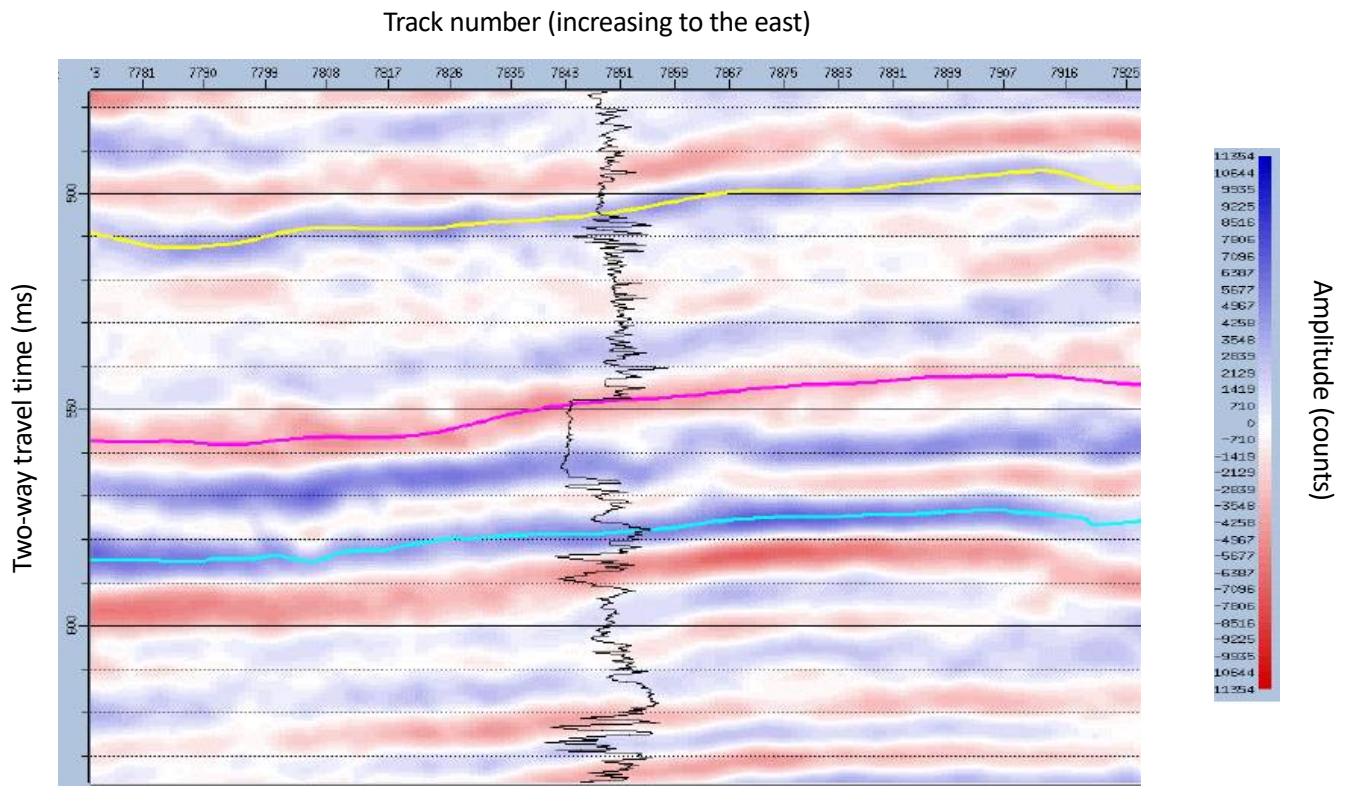
Figure 5. East-west time section through the three-dimensional seismic cube. The vertical scale show the two-way travel time in milli-seconds. The horizontal scale indicates the track number. The spacing between tracks is 10 meters. The yellow line denotes the top of the Wilrich formation. The pink curve denotes the top of the reservoir (top of the Bluesky formation). The blue curve is the base of the reservoir (top of the Debolt formation). The vertical black curve indicates the density variation as measured by a log from a well that intersects the time section. The top and base of the reservoir are clearly delineated by abrupt changes in density. The total length of this line is 1.57 km. Reprinted with permission from Shell Canada (2016).
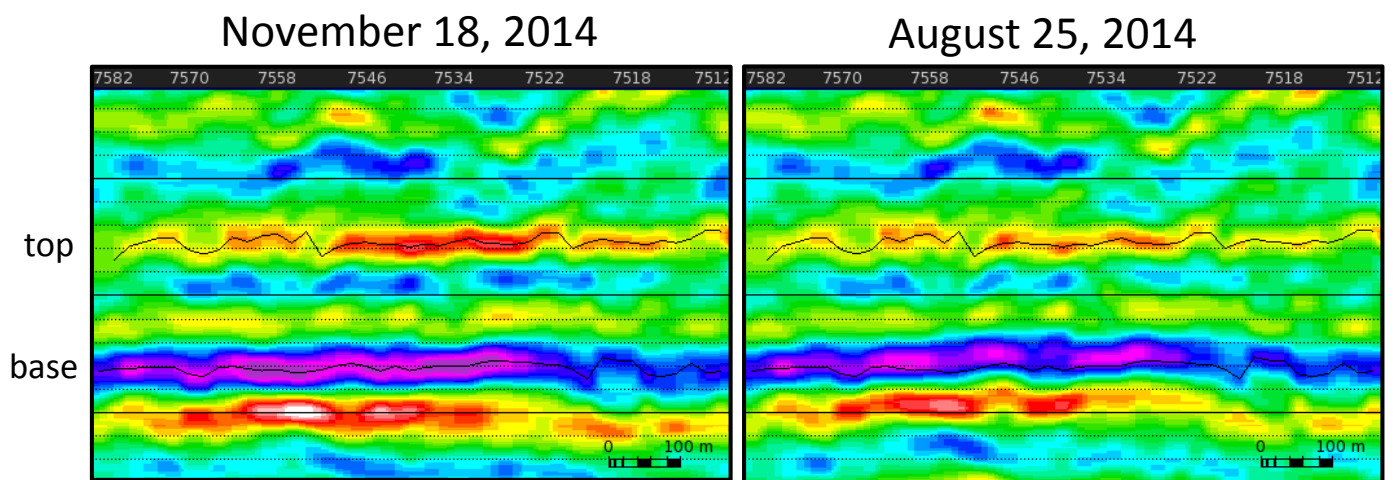
Figure 6. Two east-west cross-sections through the time-lapse seismic monitoring data. As in Figure 5, the numbers at the top of the plot are track number, spaced 10 meters apart. Coherent time shifts and amplitude changes are visible for reflections at and below the base of the reservoir. The top and base of the reservoir correspond to the pink and blue lines in Figure 5. The red values and purple values are the minimum and maximum values that lie in the range 1-2 ms. Reprinted with permission from Shell Canada (2016).
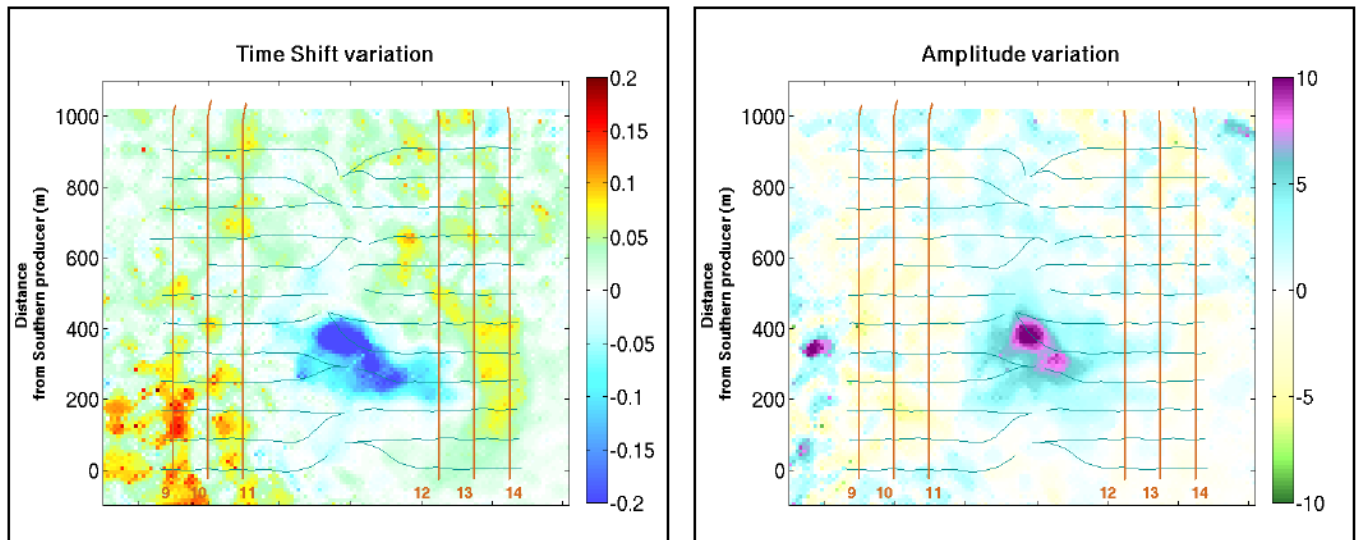
Figure 7. (Left) Time shifts for a base survey on April 14, 2014 and a monitor survey on March 30, 2015. The time-shifts are extracted using a cross-correlation technique over a 120 ms window. The pattern of travel time shifts are associated with changes due to the top-down stream drive. The time shift scale is in milli-seconds. (Right) Amplitude changes for the same baseline and monitor surveys. The amplitude changes are in percent. The vertical and horizontal axes are to the same scale. Reprinted with permission from Shell International (Shell Canada 2016).

Decreasing in the time shift can be related to the water breakthrough.

Increasing in the time shift generated by an increase in pressure, temperature or gas saturation.

Slow down

0.50
0.40
0.30
0.20
0.10
0.00
-0.10
-0.20
-0.30
-0.40
-0.50

Speed up

Time Shift Map at 8/8/15
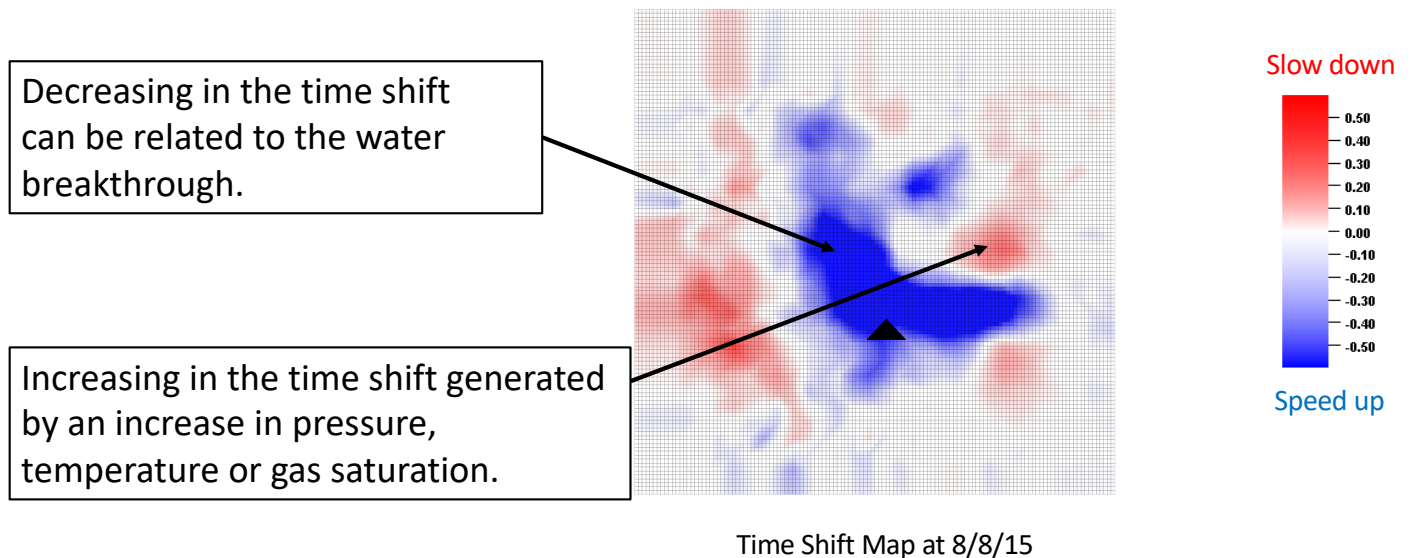
Figure 8. Interpretation of time-shift anomalies due to enhanced oil production at the Peace River field. The area shown covers the same region as that of Figure 7. The black triangle denotes the location of the set of wells (31-08) analyzed in this study. This map shows the cumulative time shifts since the start of top-down injection until August 2015. The north-south trends of positive time shifts, indicating slow down, are due to the increase in pressure and temperature associated with the overlying stream injectors. The blue anomaly indicating speed up is thought to be due to water breakthrough and filling the area containing gas, seen in Figure 4.
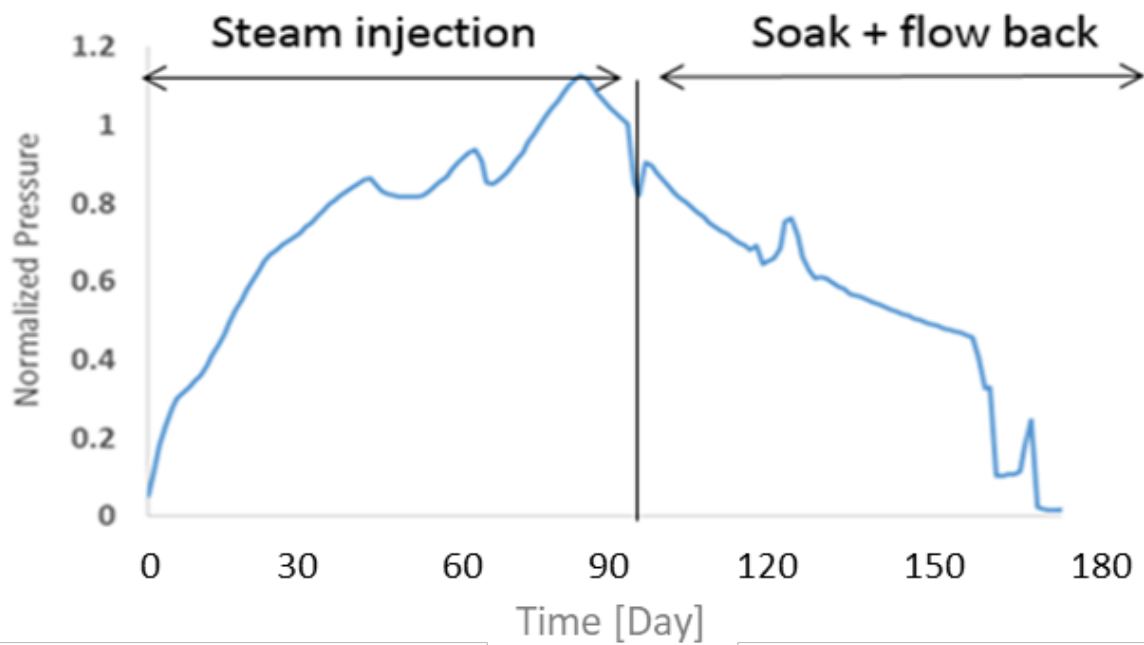
Figure 9. Normalized bottom hole pressure variation during a steam injection and production cycle that was conduct at the isolated well pattern 31-08 at the southern edge of pad 31. The production in this figure extends from August 2015 until mid-January 2016.   The peak pressure attained in the area was 7.5 MPa and the minimum pressure was slightly below 2.5 MPa.
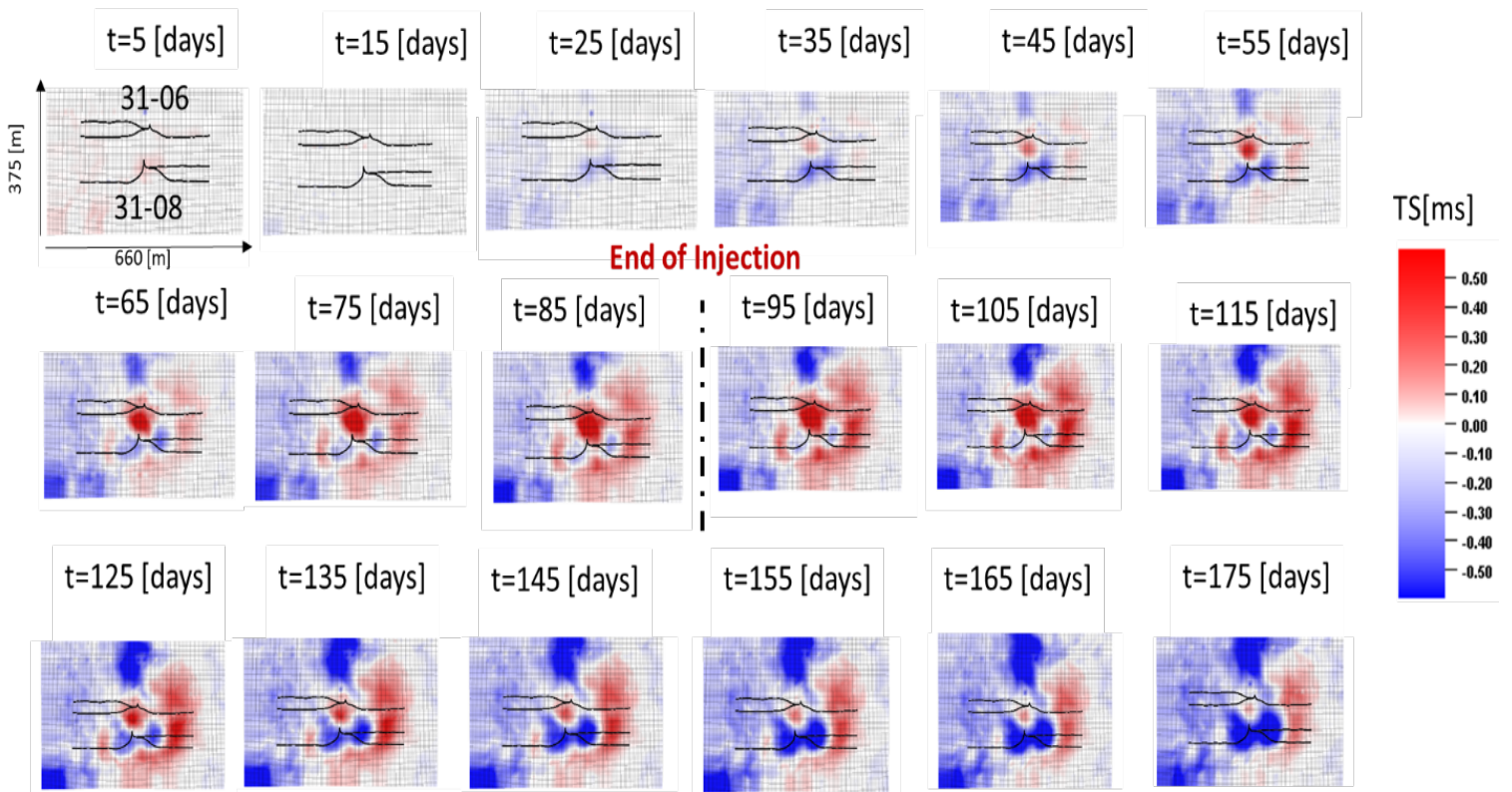
Figure 10. Seismic observations associated with the isolated cyclic steam stimulation that was conducted in well pattern 31-08, the lowermost 'tuning fork' pattern in each panel. A total of 18 time-shift maps are shown, out of the 175 available for integration. The color bar indicates the time shifts (TS) in milli-seconds.
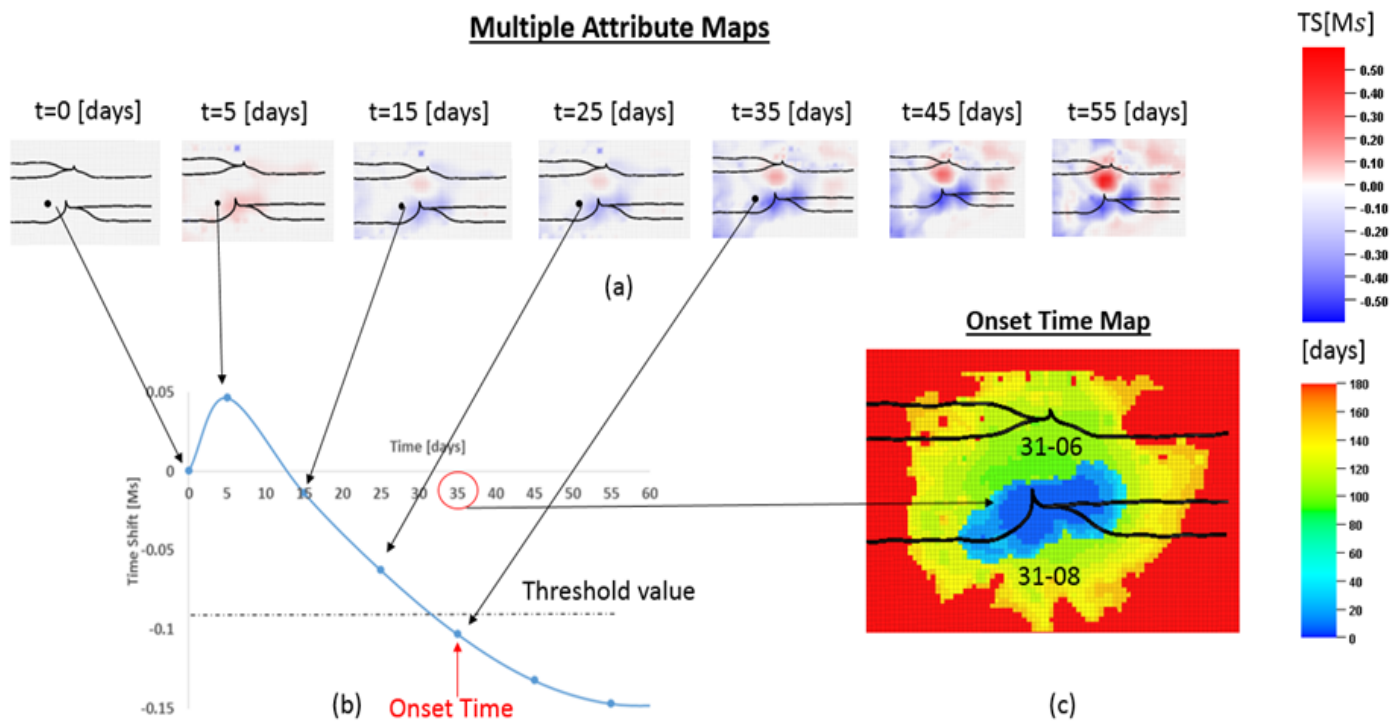
Figure 11. Conversion of multiple attribute maps (time shifts) to onset time map. (a) A sample of 7 of the 175 attribute maps that are available for integration. (b) A plot of the seismic response of a specific cell (labeled as black dot) to indicate the onset time. (c) Map obtained after converting from observed travel time shifts to estimates of onset time. The color contours display the front progression over time.
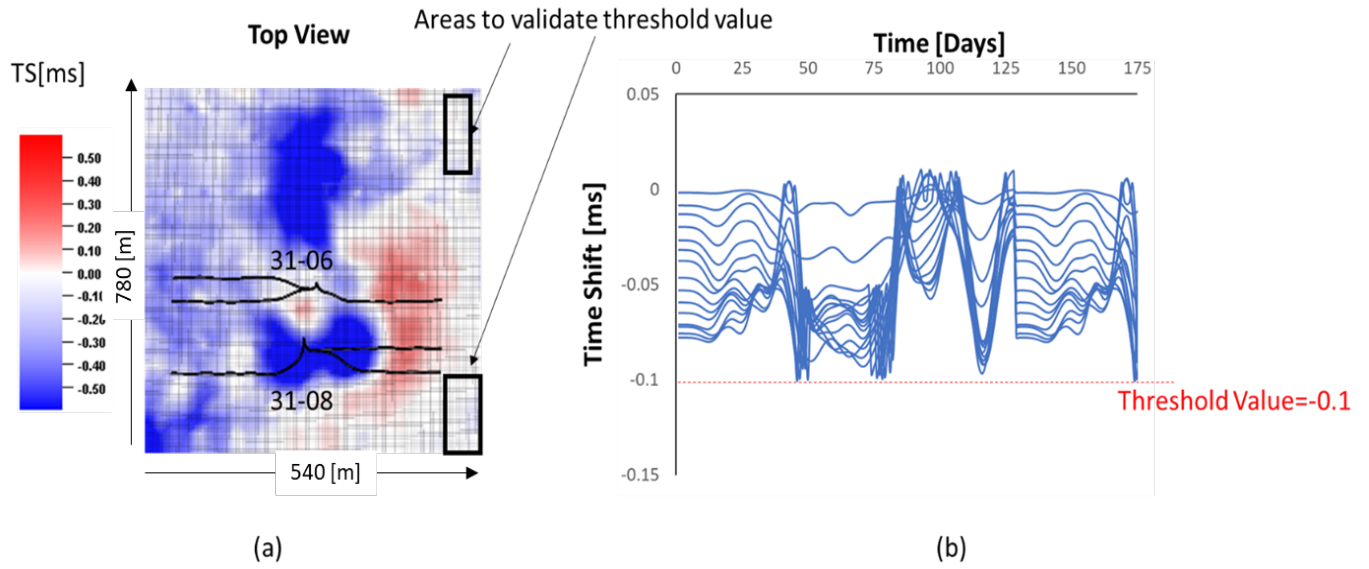
Figure 12. Validation of the defined threshold value. (a) Top view of the cross-correlation time shift map at the end of the cycle. The black squares show the sampled area. (b) Time shift plot of 200 samples over the cycle for 15 points within the two validation rectangles.
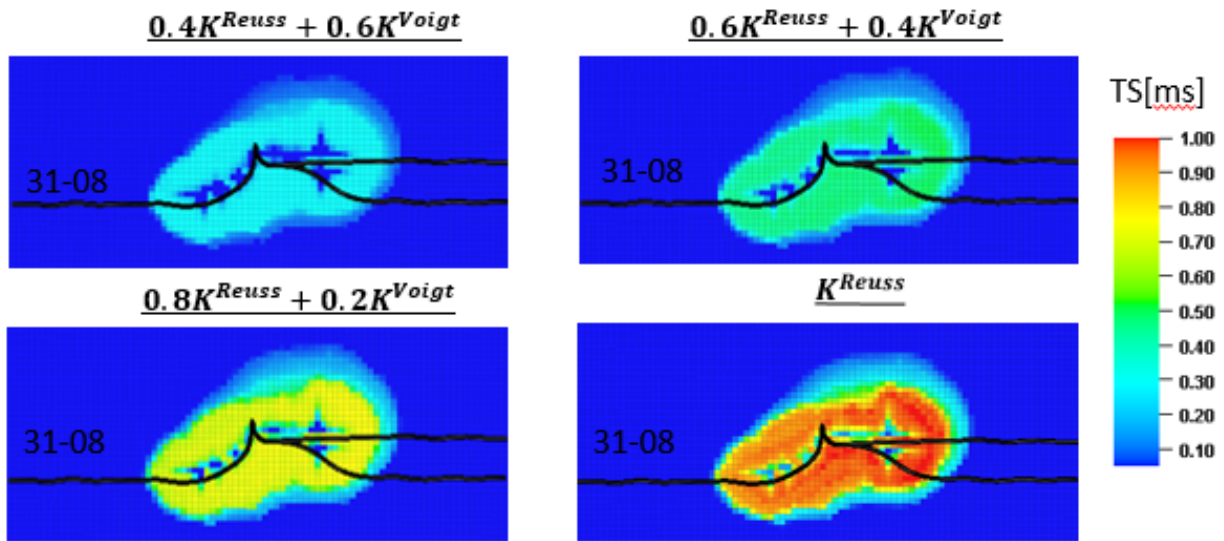
Figure 13. Time shift changes after 82 days of steam injection, calculated using four models created by a linear combination of Reuss and Voigt averages. The specific combinations are denoted in the panel titles.
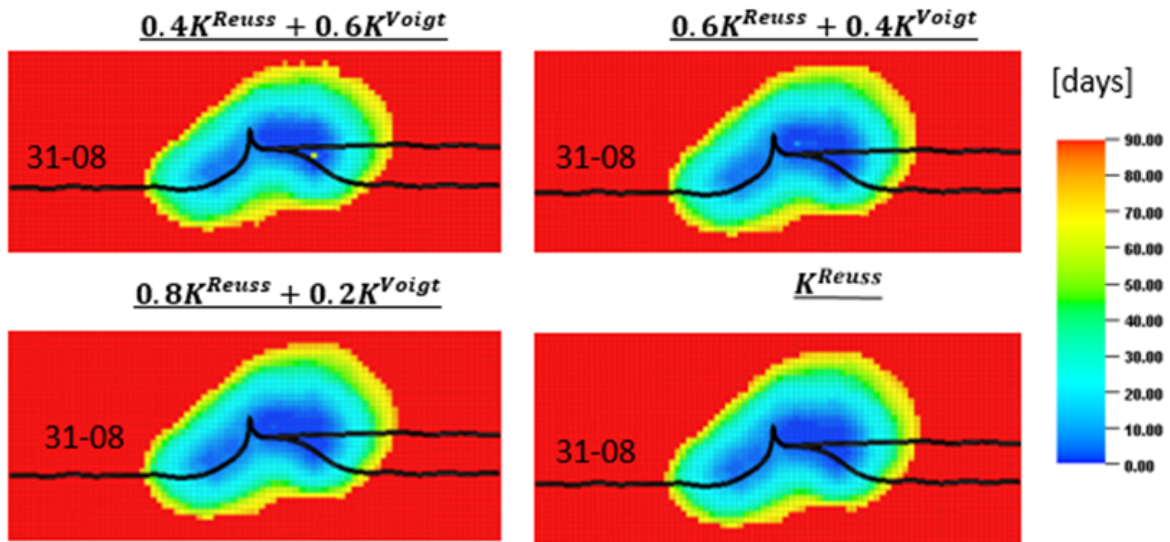
Figure 14. Onset time maps, calculated using the four models constructed by linear combinations of Reuss and Voigt averages.
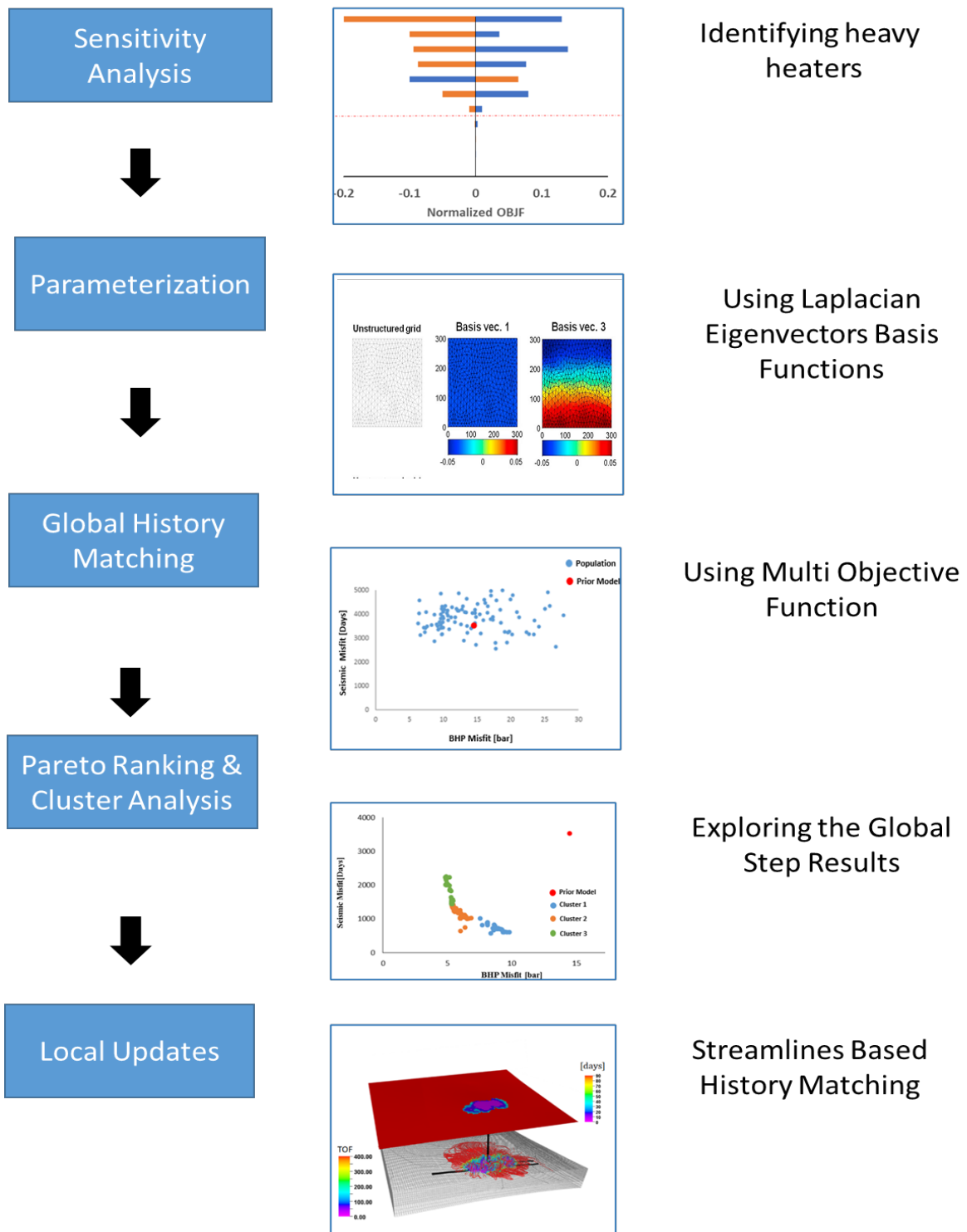
Figure 15. Flow chart of the entire inversion process.
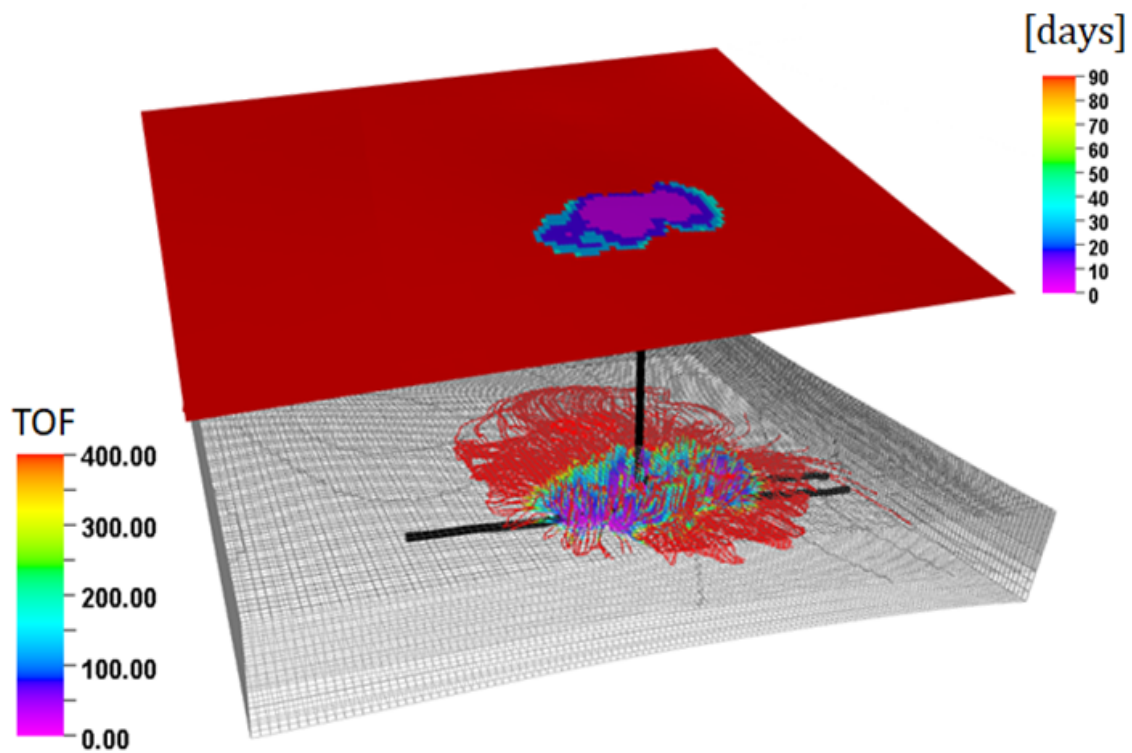
Figure 16. Streamline trajectories color coded by the time-of-flight (TOF) along the path. The time-of-flight is the travel time for a neutral tracer and is proportional to the travel time of the injected water. In order to calculate the true travel time of the water front we must multiply by the derivative of the fractional flow curve and the total mobility. The onset times of changes in the time shifts for waves propagating through the reservoir, in days since the start of injection, are plotted in the plane above the streamlines.
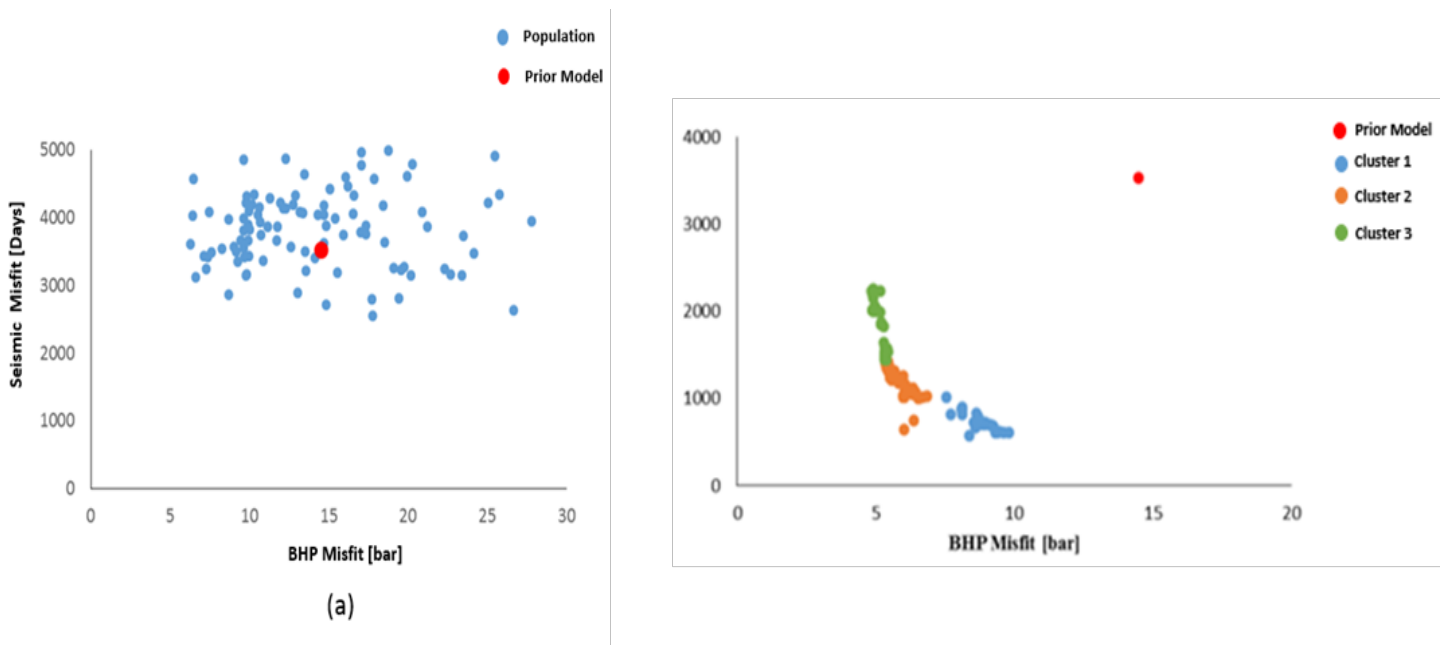
Figure 17. *(a) The seismic and bottom hole pressure misfits for 150 randomly generated initial models. (b) Models resulting from an application of the genetic algorithm that has been modified to define the Pareto front. The models are color coded to indicate clusters sharing similar characteristics.*

.

Cluster 1   Cluster 2   Cluster 3

a.   b.   c.
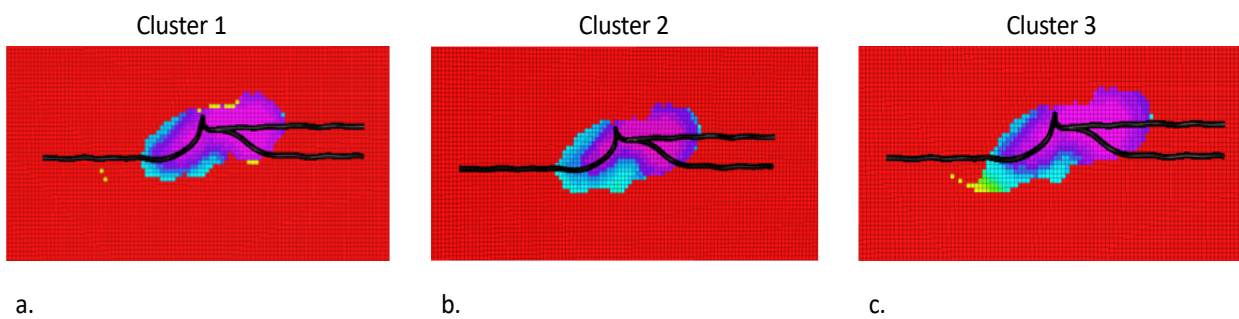
Figure 18. Onset time maps for example members of each cluster. (a) Onset time map from a member of cluster 1, (b) Onset time map from an element of cluster 2, (c) Onset time map from a solution in cluster 3. The color scale is corresponds to the color bar in Figure 16.
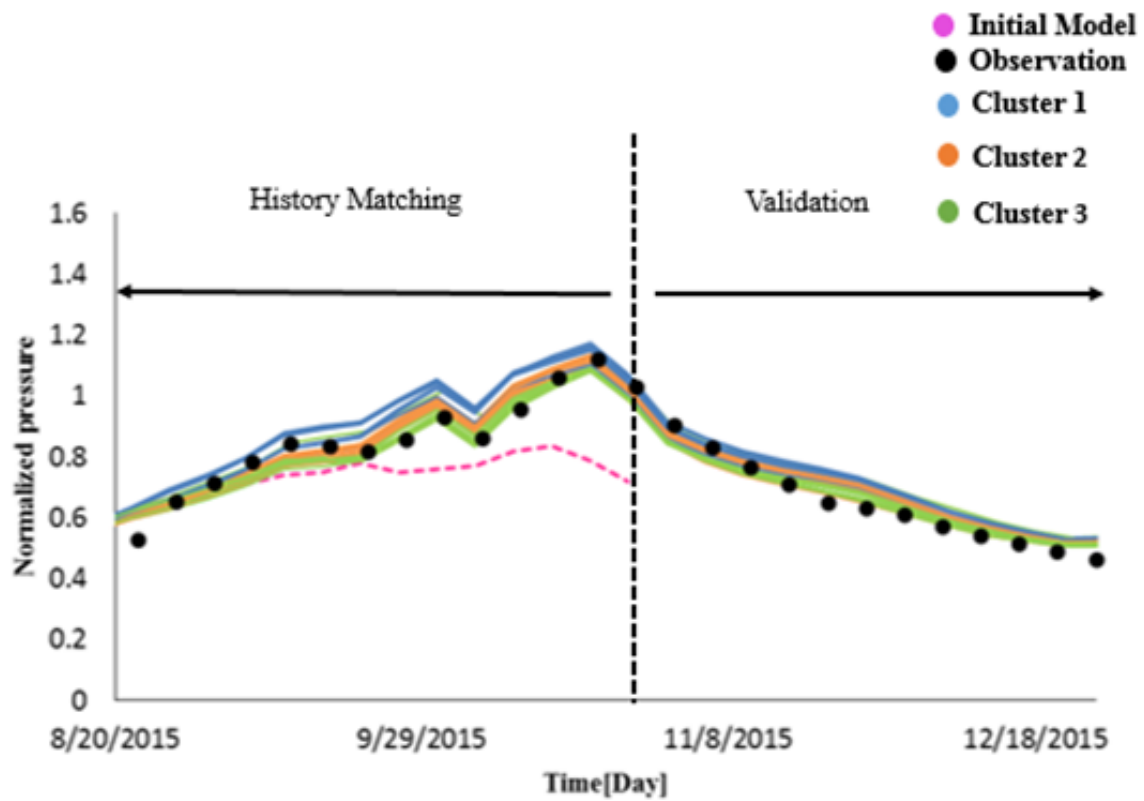
Figure 19. *Pressure response for 40 models from the final generation of the global update (colored solid lines). The initial model is indicated by the dashed pink line and the measured pressures by the black dots.*
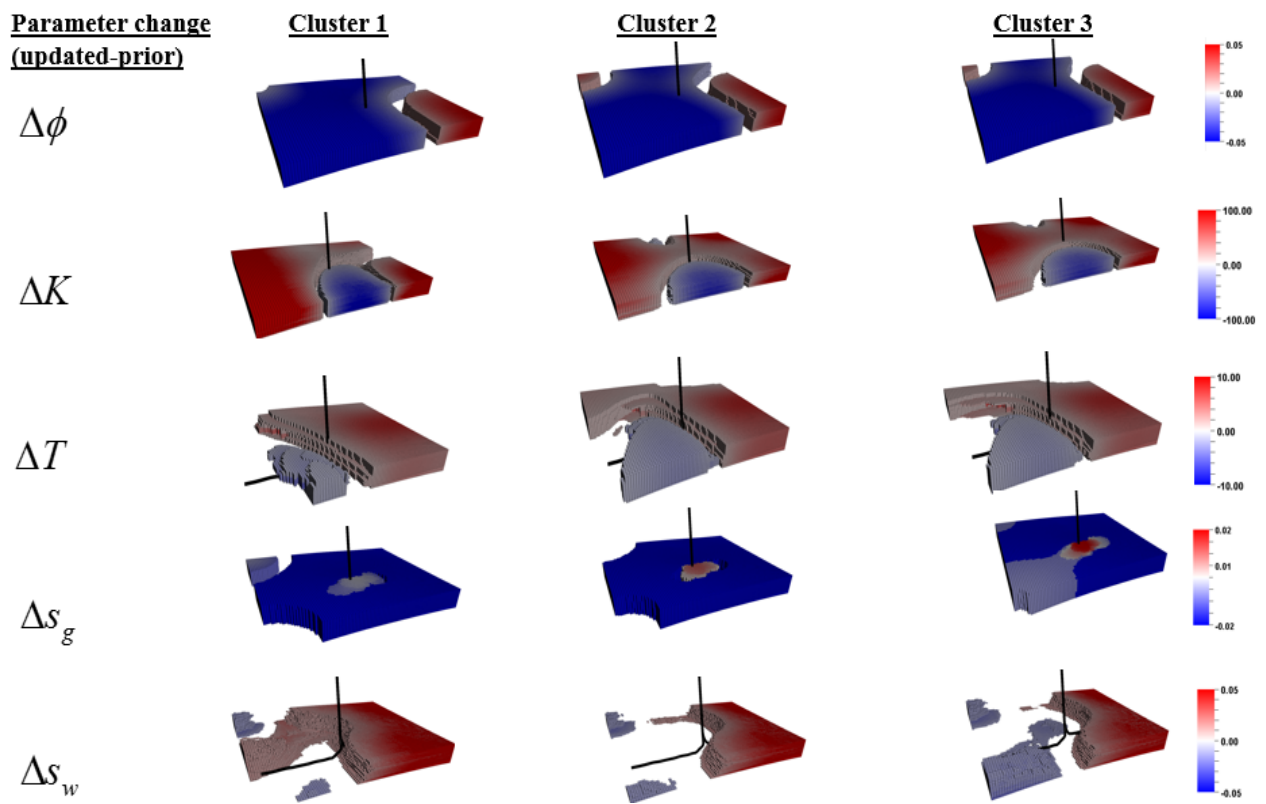
Figure 20. The change in the updated parameters after the global step for a selected model in each cluster.
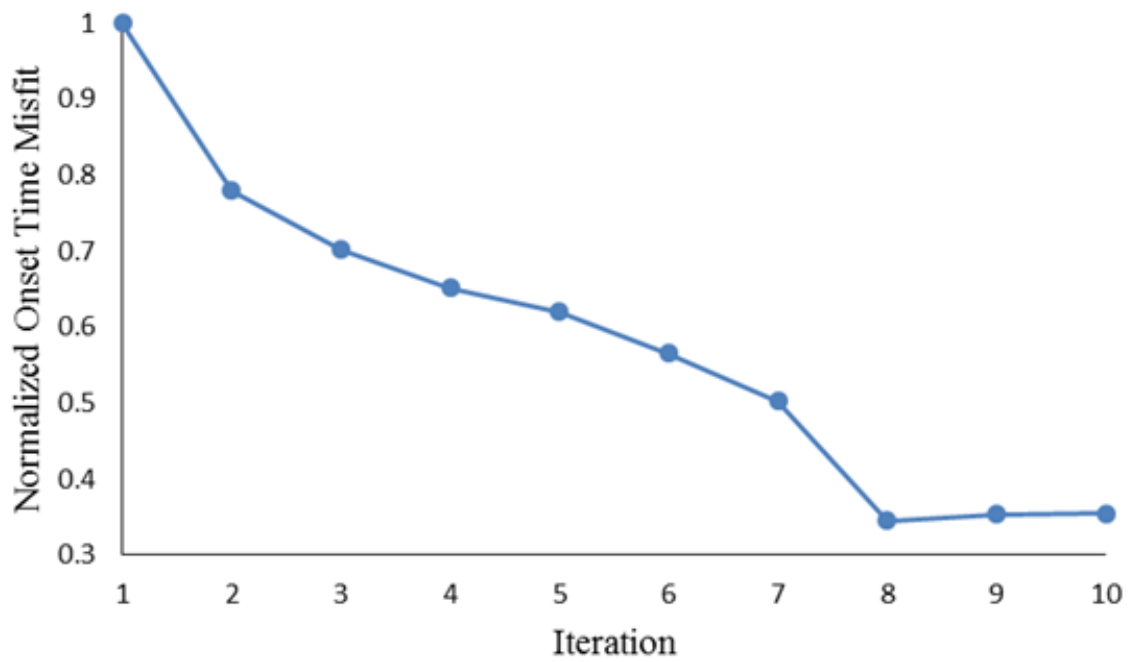
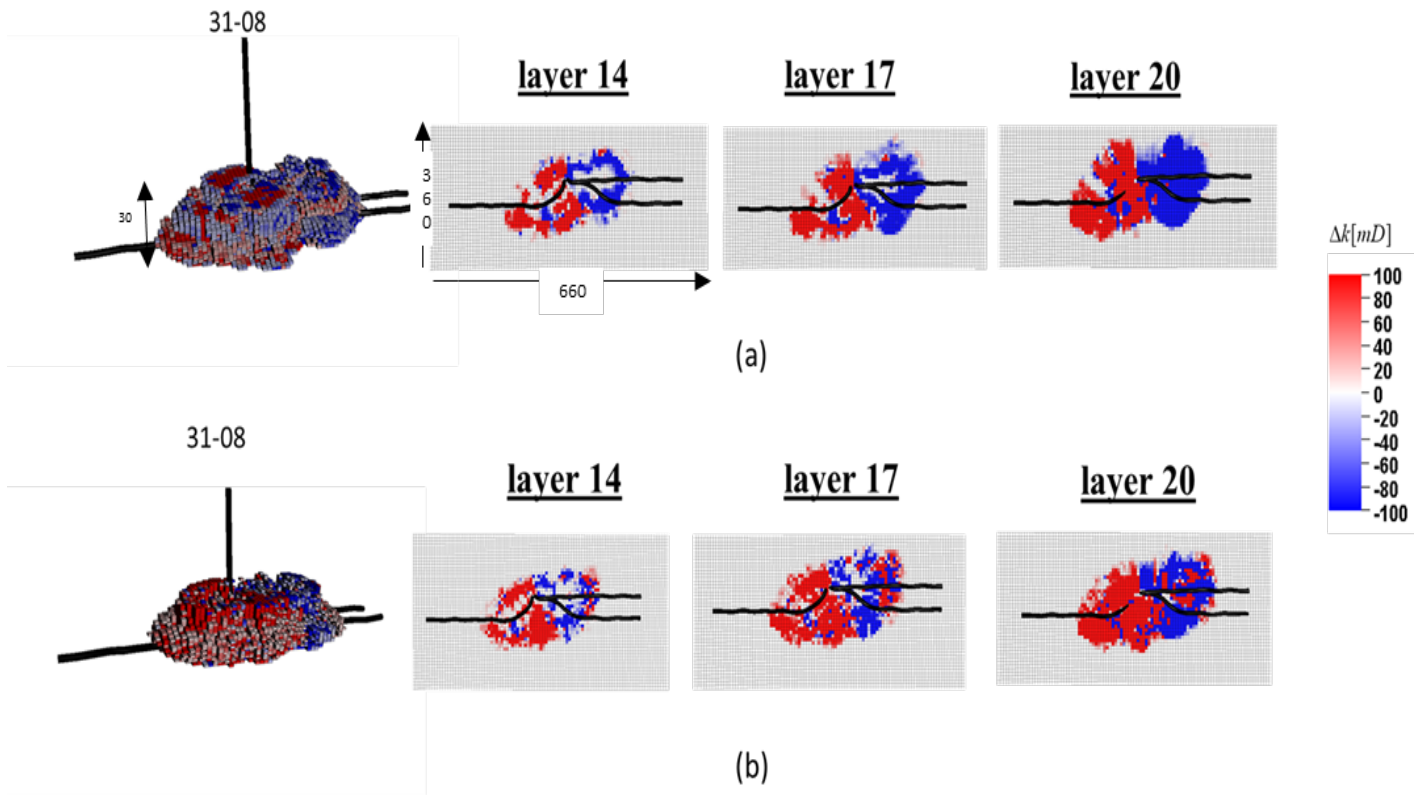*Figure 21.* Seismic data misfit as a function of the number of iterations of the inversion algorithm.

Figure 22. Permeability model change (final-prior) for a selected model. (a) model from cluster 1, and (b) model from cluster 2
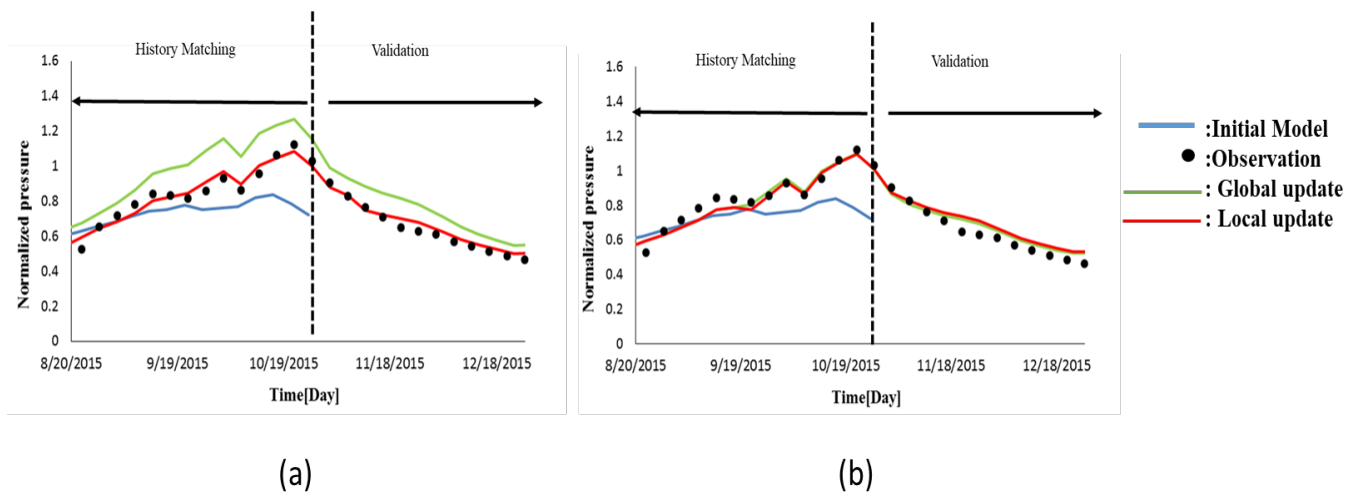
(a)   (b)

Figure 23. The BHP response of well 31-08 over the CSS cycle after the local updates for a selected model. (a) Cluster 1, and (b) cluster 2

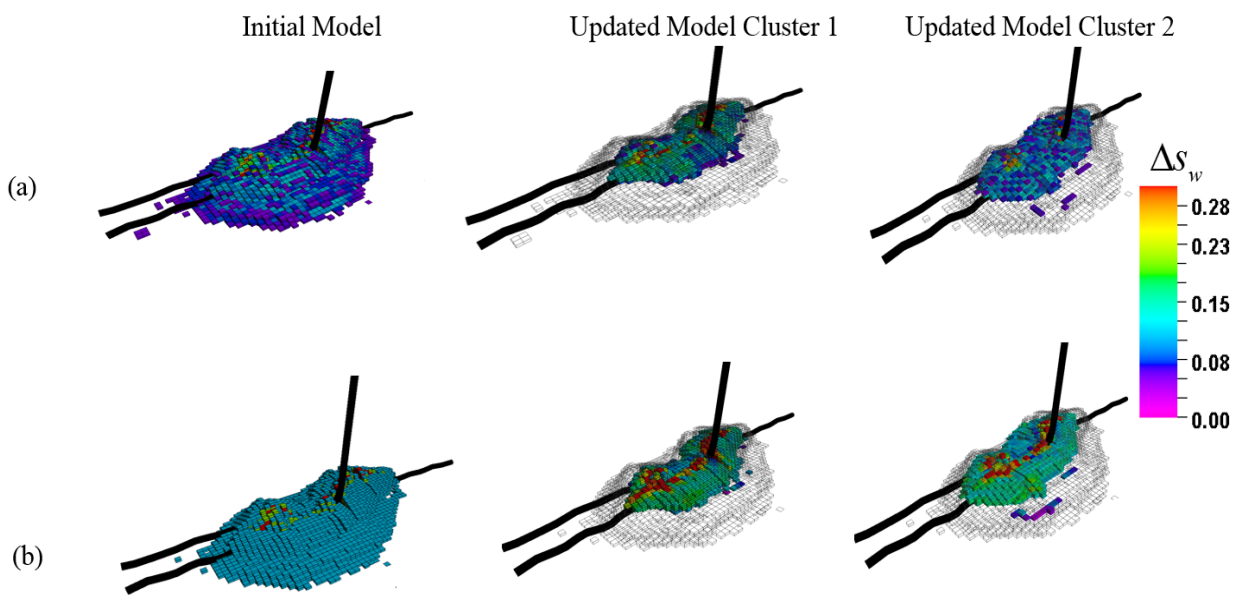*Figure 24. Water saturation change over the injection cycle for the initial and the updated models. The transparent cells in the updated models represent the water saturation changes observed in the initial model. (a) Water saturation changes after 45 days. (b) Water saturation changes after 85 days.*
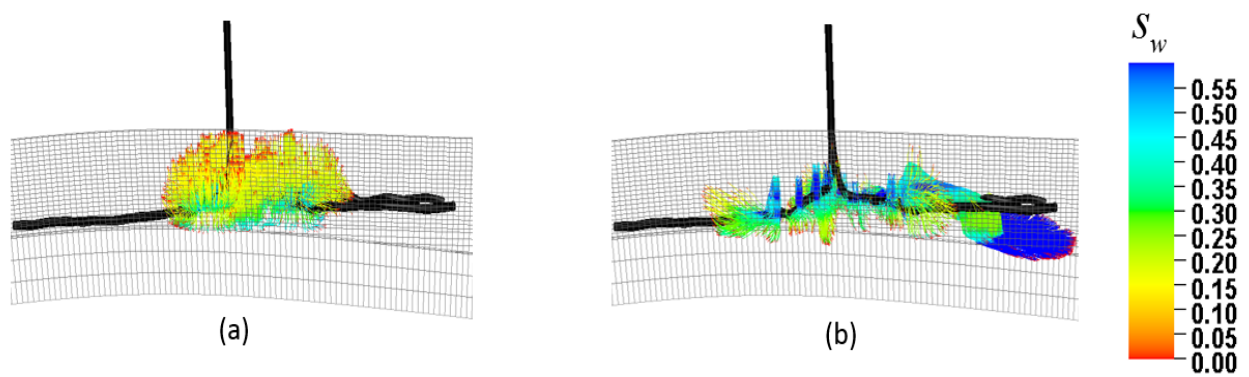
Figure 25. Cross-sectional view of the water saturation along the streamlines over the injection interval. (a) Water saturation along the streamlines after 5 days, and (b) water saturation along the streamlines after 80 days.
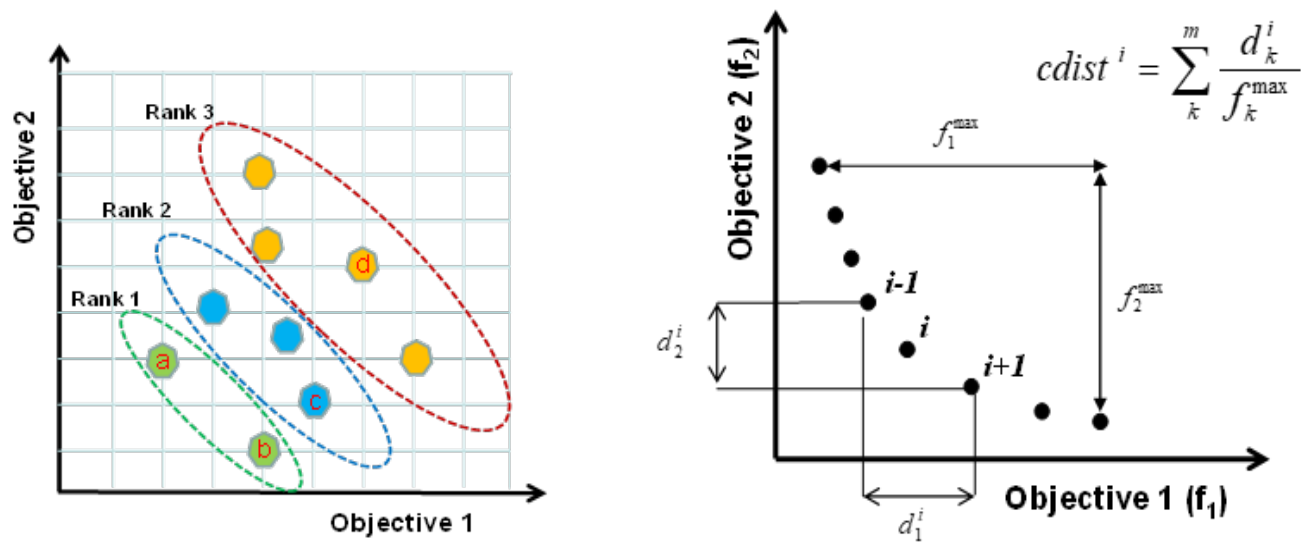
$$cdist^{i} = \sum_{k}^{m} \frac{d^{i}_{k}}{f^{max}_{k}}$$

Figure B1. Illustration of the ranking of models (left panel) and the crowding distance for the i-th solution, cdist^{i} (right panel).